SEDIMENTOLOGY the journal of the International Association of Sedimentologists

Sedimentology (2018) doi: 10.1111/sed.12453

Geometry and dynamics of braided channels and bars under experimental density currents

AJAY B. LIMAYE*, JEAN-LOUIS GRIMAUD*,[1], STEVEN Y. J. LAI†, BRADY Z. FOREMAN‡, YUHEI KOMATSU§ and CHRIS PAOLA*

**Department of Earth Sciences, St. Anthony Falls Laboratory, University of Minnesota, Minneapolis, MN 55455, USA (E-mail: aslimaye@umn.edu)*

†Department of Hydraulic and Ocean Engineering, National Cheng Kung University, No. 1 Daxue Road, East District, Tainan City, Taiwan 701

‡Department of Geology, Western Washington University, 516 High Street, Bellingham, WA 98225, USA

§Technology Research, Japan Oil, Gas and Metals National Corporation, 1-2-2 Hamada, Mihama-ku, Chiba-city, Chiba 261-0025, Japan

Associate Editor – Jaco Baas

ABSTRACT

Submarine channels convey turbidity currents, the primary means for distributing sand and coarser sediments to the deep ocean. In some cases, submarine channels have been shown to braid, in a similar way to rivers. Yet the strength of the analogy between the subaerial and submarine braided channels is incompletely understood. Six experiments with subaqueous density currents and two experiments with subaerial rivers were conducted to quantify: (i) submarine channel kinematics; and (ii) the responses of channel and bar geometry to subaerial versus submarine basin conditions, inlet conditions and the ratio of 'flow to sediment' discharge (Q_w/Q_s). For a range of Q_w/Q_s values spanning a factor of 2·7, subaqueous braided channels consistently developed, were deeper upstream compared to downstream, and alternated with zones of sheet flow downstream. Topographic analyses included spatial statistics and mapping bars and channels using a reduced-complexity flow model. The ratio of the estimated depth-slope product for the submarine channels versus the subaerial channels was greater than unity, consistent with theoretical predictions, but with downstream variations ranging over a factor of 10. For the same inlet geometry and Q_w/Q_s, a subaqueous experiment produced deeper, steeper channels with fewer channel threads than its subaerial counterpart. For the subaqueous cases, neither slope, nor braiding index, nor bar aspect ratio varied consistently with Q_w/Q_s. For the subaqueous channels, the timescale for avulsion was double the time to migrate one channel width, and one-third the time to aggrade one channel depth. The experiments inform a new stratigraphic model for submarine braided channels, wherein sand bodies are more laterally connected and less vertically persistent than those formed by submarine meandering channels.

Keywords Braided rivers, experiments, landscape evolution, morphodynamics, stratigraphy, turbidity currents.

[1]Present address: MINES ParisTech, PSL Research University, Centre de Géosciences, 35 rue Saint Honoré 77305, Fontainebleau, France.

INTRODUCTION

Turbidity currents are subaqueous gravity flows in which turbulence holds sediment in suspension. In ocean basins, turbidity currents result from mass movements and hyperpycnal flows (Normark & Piper, 1991; Mulder & Syvitski, 1995; Piper & Normark, 2009). Turbidity currents represent the main mechanism by which clastic sediment, delivered to shallow water by fluvial transport, reaches the deep ocean (Normark & Reid, 2003; Romans *et al.*, 2009). Turbidites record continental denudation over million-year timescales (Métivier *et al.*, 1999; Molnar, 2004) and are major hydrocarbon reservoirs (Weimer & Link, 1991).

The channels that convey turbidity currents are commonly sinuous and have a single thread (Flood & Damuth, 1987; Clark *et al.*, 1992; Deptuck *et al.*, 2007). Apparently multi-thread channels are rarer on the modern sea floor (Walker, 1978; Hein & Walker, 1982; Cronin & Kidd, 1998; Rotzien *et al.*, 2014). Proposed modern examples of braiding occur on submarine fans in the Orinoco (Fig. 1A), Var, Monterey, and Santa Monica basins (Belderson *et al.*, 1984; Hesse *et al.*, 2001; Callec *et al.*, 2010), and the Bering, Labrador (Fig. 1B) and Tyrhennean seas (Fig. 1C) (Kenyon & Millington, 1995; Hesse *et al.*, 2001; Gamberi & Marani, 2011). Several studies have used rivers as a template for interpreting submarine meandering channels and their deposits (Pirmez & Imran, 2003; Jobe *et al.*, 2016). In comparison, few studies have tested the strength of the analogy between submarine and subaerial braided channels.

The geometry of river and submarine channels, and their movement across braid plains and floodplains, leave lasting imprints in stratigraphy. For example, channel aggradation can form sand bodies that are well-connected vertically and longitudinally at the scale of a channel thread (Willis, 1993; Peakall *et al.*, 2000; Jerolmack & Mohrig, 2007; Jobe *et al.*, 2016). Sand bodies can occur in isolation, however, owing to avulsions that displace channels by distances much greater than the channel width (Leeder, 1977; Allen, 1979; Bridge & Mackey, 1993; Hajek *et al.*, 2010).

Experiments offer a means to compare the development of channels, bars and stratigraphy between subaerial (Ashmore, 1982; Moreton *et al.*, 2002; Bertoldi *et al.*, 2009; Tal & Paola, 2010) and submarine environments. Erosional and depositional channels can spontaneously develop under subaqueous conditions (Métivier *et al.*, 2005; Yu *et al.*, 2006; Foreman *et al.*, 2015). The experiments by Foreman *et al.* (2015) indicated that submarine braided channels form under high flow width to depth ratios (i.e. >100), similar to fluvial channels (Parker, 1976). This finding represents a step towards developing stratigraphic models for deposits generated by submarine braided channels. To proceed further, such models require constraints on the

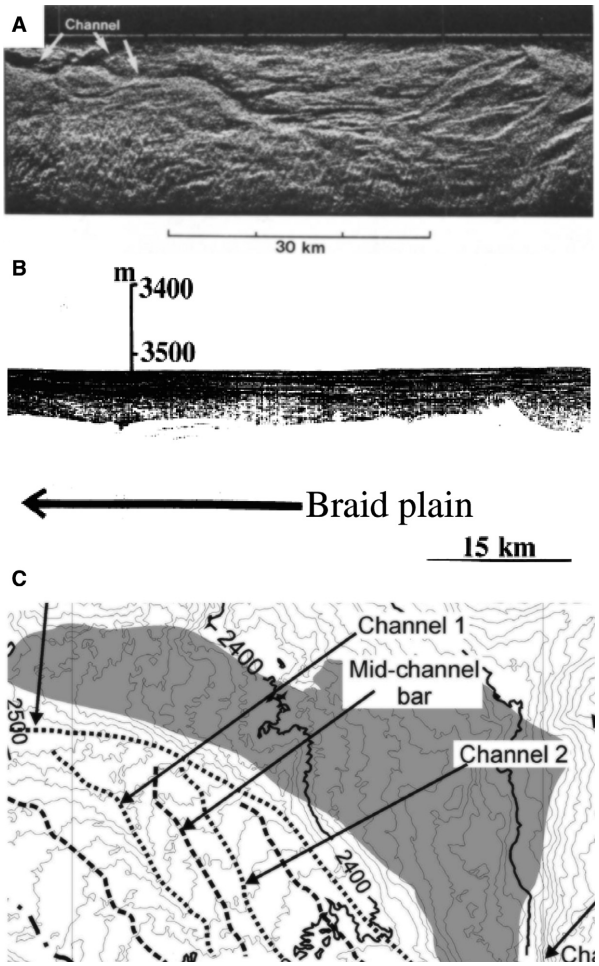

Fig. 1. Natural settings where submarine braiding has been suggested or described. (A) Sonar image of the Orinoco submarine fan [12° N, 57° W reproduced from Belderson *et al.* (1984) with permission from Elsevier]. Arrows denote interpreted channels. (B) Cross-section of seafloor sediments imaged with sonar and previously interpreted as a braid plain [57° N, 50° W reproduced from Hesse *et al.* (2001) with permission from the American Association of Petroleum Geologists]. (C) Contour map of bathymetry for the Tyrrhenian Sea (39·9° N, 15·3° E), including interpreted channels (thin dashed lines) and a mid-channel bar (thick dashed lines). Numbers indicate depths in metres. Reproduced from Gamberi & Marani (2011).

geometry of bars and channels, and the shifting of these elements that sets their arrangement in larger-scale reservoirs. The scales of coarse-sediment connectivity within deposits formed by submarine braided channels are largely unconstrained.

In this paper three factors are hypothesized to influence channel and bar formation: (i) the ratio of flow discharge (Q_w) to sediment discharge (Q_s); (ii) the geometry of the source of water and sediment; and (iii) the density contrast that distinguishes the subaqueous and subaerial flow environments. These variables are discussed in turn. First, the discharge ratio (Q_w/Q_s) sets slope in depositional settings (Paola, 2000). Ashworth *et al.* (2007) further suggested that changes in Q_w/Q_s cause subaerial braided channels to adjust their planform morphology, including the number of channel threads that transport sediment. Experiments by Egozi & Ashmore (2008, 2009) and Bertoldi *et al.* (2009) show that braided channels increase the number of inundated channels in a cross-section following an increase in water discharge. A similar planform response is hypothesized to occur for submarine channels.

Second, the geometry of the source of flow and sediment may also influence bar and channel formation. Experimental density currents are often wall-bounded, or introduced directly to pre-formed, single-thread channels (Marr *et al.*, 2001; Peakall *et al.*, 2007; Straub *et al.*, 2008). Cases with self-formed channels typically use a single inlet condition, either as a point source (Métivier *et al.*, 2005; Yu *et al.*, 2006; Rowland *et al.*, 2010) or a distributed (line) source, where water and sediment are fed across the full width of the basin (Foreman *et al.*, 2015; Lai *et al.*, 2017). The former resembles the apex of a distributary network, whereas the latter approximates the spatially averaged discharge of water and sediment across a developed braid plain. All of the aforementioned experiments generated channels, but the influence of inlet conditions on bar and channel geometry has not been quantitatively tested.

Third, as described below, theory suggests that channel depth and/or slope is larger in the submarine case for the experiments. For braided rivers, channel depth represents the distance between channel beds and bar tops, and scales the elevation distribution (Redolfi *et al.*, 2016). In submarine channels, bar heights can be substantially less than the flow and channel depth (Abreu *et al.*, 2003; Wynn *et al.*, 2007; Nakajima *et al.*, 2009). Nonetheless, larger channel depths in the submarine case are hypothesized to produce larger topographic variations compared to the subaerial case.

This study focuses on a new set of experiments that test the conditions favourable to submarine braiding, assess controls on channel and bar geometry, and relate channel kinematics to deposit architecture. To test hypothesis 1, the flow and sediment discharges are changed as independent variables in the experiments. To test hypothesis 2, the experiments use each of the two end-member conditions (point source and line source) for introducing water and sediment. To test hypothesis 3, control experiments are run under subaerial conditions to relate subaqueous and subaerial geometries under similar experimental conditions.

EXPERIMENT DESIGN AND SPATIAL ANALYSIS

Experiment design

Fine sediments abound in marine stratigraphy, and sediment suspension plays a key role in turbidity current dynamics (Kuenen, 1951; Middleton, 1967; Straub *et al.*, 2008). By analogy to braided rivers, however, relatively coarse sediment that travels primarily as bedload is hypothesized as the main control on bar construction and submarine braiding. Therefore, the experiments use sand and exclude sediment settling from suspension. Table 1 shows the grain-size distribution, which is unimodal; 80% of grain diameters fall between 0·250 mm and 0·420 mm. The mean and maximum of these bounds, respectively, are used to estimate D_{50} = 0·33 mm and D_{90} = 0·42 mm. The sediment is composed of non-cohesive, plastic (Plasti-Grit™) grains, whose low density (1·22 to 1·32 g cm^{-3}) compared to natural sediment reduces the critical shear stress for motion.

Table 1. Grain-size distribution for the plastic sediment.

Grain diameter (mm)	Percent finer
0·149	0
0·250	9
0·420	89
0·595	99

The density currents were supplied continuously to constrain dynamics of channel shifting during aggradation (Métivier *et al.*, 2005; Yu *et al.*, 2006; Foreman *et al.*, 2015; Lai *et al.*, 2017). Dissolved salt provides the excess density to the flow (Laval *et al.*, 1988; García & Parsons, 1996; Foreman *et al.*, 2015). In comparison to a flow with suspended sediment, the salt-water solution does not obscure the bed, and has a density that is more easily controlled and raised to sustain stratification.

All experiments occurred in a custom-built flume (Fig. 2). The flume rests in a basin 1·0 m wide, 0·5 m deep and *ca* 4·0 m long, and includes three sections of differing downstream slope (Fig. 2A). From upstream to downstream, these sections are the inlet (10° slope, 30 cm length), main (2° slope, 185 cm length) and end section (approximately horizontal, 50 cm length). The slope breaks allow a deposit several centimetres thick to accumulate atop the main section.

For the submarine experiments, the basin was filled with fresh water to inundate all three sections (Fig. 2A). The solution was introduced at the upstream end of the basin. Two inlet conditions for flow and sediment were tested. For the first case, defined as the line source inlet condition (Fig. 2A), salt water was introduced to a reservoir at the upstream end of the flume. Upon overtopping the reservoir, the solution flowed as an undercurrent across the flume bed. Sediment was introduced from two sediment feeders and distributed across the width of the main section at the spill-over point using attachments at the feeder nozzles. The sediment settled until entrained by the salt-water current. In the second inlet condition, defined as a point source (Fig. 2B), salt water and sediment entered the flume as an expanding flow. For both inlet conditions, the salt-water current continued along the flume surface and deposited most of the sediment within the main section. The current then spilled over a third and final slope break to a deep sump and was removed by a pump, which regulated the depth and salinity of the ambient water. Dye was added intermittently to the inflow for visualization.

The salt water had a density of $1{\cdot}20 \pm 0{\cdot}05$ g cm^{-3}, and thus an initial excess density of 20% compared to the ambient water. The salinity of the ambient water increased gradually due to salt-water mixing. Therefore, the experiment was stopped at regular intervals to slowly drain and refill the fresh water in the basin. This process caused no observable change in the density current behaviour and no significant topographic change.

The experiments also included subaerial control runs using both inlet conditions. Figure 2C shows a schematic of the subaerial configuration for the line source inlet condition, which used a fresh water source. For the subaerial experiments, the water filling the basin was lowered to the termination of the end section, and acted as a fixed base-level during each run.

A fixed overhead camera acquired photographs every minute. An optical laser-line scanner generated digital elevation models (DEMs) with sub-millimetre vertical precision and millimetre grid spacing. For the subaerial experiments, topography scans occurred at 15 to 30 min intervals. Due to refraction effects, topography data was not collected while the experiment was inundated. Therefore, the topographic scans were more intermittent (i.e. one to two hour intervals) for the submarine experiments. All experiments ran for several hours (Table 2) and were stopped when sediment back-filled the inlet. A fraction of the introduced sediment accumulated near the inlet or accumulated in the deep sump, and was removed by hand.

Five of the experiments used the same value of $Q_w/Q_s \cong 10$, but different combinations of basin conditions and inlet conditions, and different discharge magnitudes. The remaining experiments varied salt-water discharge (for the submarine experiments), fresh-water discharge (for the subaerial experiments) and sediment discharge. Water discharge was varied from 0·035 to 0·065 L s^{-1}, while sediment discharge was varied from 0·0023 to 0·0046 L s^{-1}, resulting in a range of Q_w/Q_s from 10·0 to 27·2 (Table 2). Mean water and sediment discharge were fixed for each experiment, but water discharge varied by *ca* 20% due to pump fluctuations. Within the range of Q_w/Q_s, sediment moved without fully bypassing the main section.

The total run time varied from 120 to 750 min (Table 2), and reflected the time for sediment to back-fill the inlet. Time is non-dimensionalized using the equation:

$$t^* = \frac{Q_s t}{D_{50}^3} \tag{1}$$

where t is time and D_{50} is median grain diameter. Between experiments, the maximum value

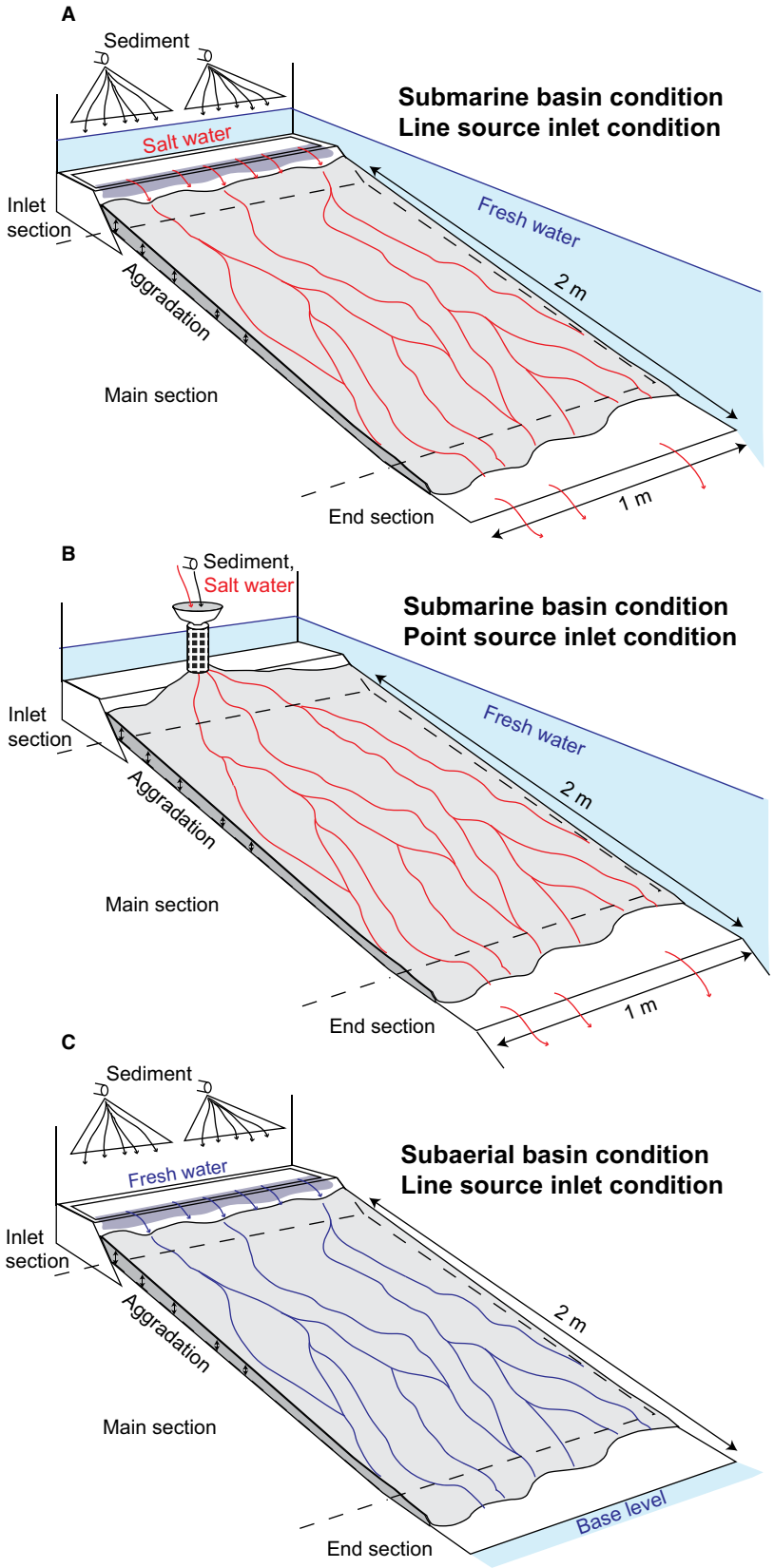

Fig. 2. Schematics of experiment configuration. (A) Submarine basin condition a line source of water and sediment. (B) Submarine basin condition with a point source of water and sediment. (C) Subaerial basin condition, with base level fixed at the end of the main section, and a line source of water and sediment.

Table 2. Experiment parameters, including flow and sediment discharge (Q_w and Q_s, respectively), time (t), and dimensionless time ($t^* = tQ_s/D_{50}^3$, where D_{50} is median sediment grain diameter).

Experiment	Basin condition	Inlet condition	t (min)	Q_w (L/s)	Q_s (L/s)	Q_w/Q_s	t^*
Submarine 1	Submarine	Line	250	0·046	0·0046	10·0	$1·92 \times 10^9$
Submarine 2	Submarine	Line	360	0·046	0·0023	20·0	$1·38 \times 10^9$
Submarine 3	Submarine	Line	750	0·0625	0·0023	27·2	$2·88 \times 10^9$
Submarine 4	Submarine	Line	300	0·035	0·0035	10·0	$1·75 \times 10^9$
Submarine 5	Submarine	Point	210	0·065	0·0035	18·6	$1·22 \times 10^9$
Submarine 6	Submarine	Point	120	0·035	0·0035	10·0	$7·01 \times 10^8$
Subaerial 1	Subaerial	Line	270	0·0466	0·0046	10·1	$3·18 \times 10^9$
Subaerial 2	Subaerial	Point	705	0·0371	0·0035	10·6	$5·41 \times 10^9$

of t^* varied from $7·01 \times 10^8$ to $5·41 \times 10^9$ (Table 2).

Scaling

Table 3 summarizes flow and sediment transport parameters. The input parameters include slope (S), flow velocity (u), flow depth (h) and, for the submarine basin condition, the bulk densities of the current (ρ_c) and the ambient fluid (ρ_a). For simplicity, these values were estimated based on the initial condition of the experiments, with flow and sediment moving across the bare basin surface.

The slope (S = 0·035) corresponds to the main section of the basin without sediment (Fig. 2A). Flow velocity was estimated by observing the transit time of the dyed flow from the inlet to the terminus of the end section. Flow depth was estimated by spot measurements using a ruler immediately downstream of the inlet section. With these simple measurements, no systematic difference was observed between the depth and velocity of the subaerial and submarine flows as they entered the basin. Therefore, the estimated velocity (u = 1 cm s^{-1}) and flow depth (h = 2 mm) were used for the calculations in this section.

The non-dimensional parameters include the conventional Froude number ($\mathrm{Fr} = u/(gh)^{1/2}$), where g is gravitational acceleration; densimetric Froude number ($\mathrm{Fr_d} = u/(g'h)^{1/2}$), where g' is reduced gravity and $g' = g(\rho_c - \rho_a)/\rho_c$; bulk Reynolds number ($\mathrm{Re} = uh/\upsilon$), where $\upsilon = 10^{-6}$ m^2 s^{-1} is the kinematic viscosity of water and the effect of dissolved salt on viscosity is neglected; and particle Reynolds number is calculated as $\mathrm{Re_p} = u_\tau D_{90}/\upsilon$, where $u_\tau = (g'hS)^{1/2}$ is the shear velocity and the length scale for bed roughness is set as the diameter of coarse sediments (i.e. D_{90}; Peakall *et al.*, 1996). Shear velocity in turbidity currents is commonly calculated using turbulent kinetic energy (e.g. Parker *et al.*, 1987; Huang *et al.*, 2005) but the approach adopted here does not require velocity measurements.

Table 3. Characteristic dimensional and non-dimensional parameters for the submarine and subaerial experiments. The parameters include the characteristic flow velocity (u), flow depth (h), median sediment grain diameter (D_{50}), gravitational acceleration (g), and the densities of sediment, the current and the ambient fluid (ρ_s, ρ_c and ρ_a, respectively). The dimensionless parameters are the conventional Froude number [$\mathrm{Fr} = u/(gh)^{1/2}$; densimetric Froude number ($\mathrm{Fr_d} = u/(g'h)^{1/2}$), where $g' = (\rho_c - \rho_a)/\rho_c$)]; bulk Reynolds number ($\mathrm{Re} = uh/\upsilon$, where υ is the kinematic viscosity of fresh water); particle Reynolds Number ($\mathrm{Re_p} = u_\tau D_{90}/\upsilon$, where $u_\tau = (g'hS)^{1/2}$ is shear velocity); and Shields number. The latter is $\tau^*_{sa} = hS/RD_{50}$ for the subaerial case, where $R = (\rho_s - \rho)/\rho$; and $\tau^*_{sm} = hS/R'D_{50}$ for the submarine case, where $R' = (\rho_s - \rho_c)/(\rho_c - \rho_a)$.

	Submarine experiments	Subaerial experiments
Dimensional parameters		
u (cm s^{-1})	1	1
h (mm)	2	2
D_{50} (mm)	0·33	0·33
D_{90} (mm)	0·42	0·42
S	0·035	0·035
ρ_s (g cm^{-3})	1·27	1·27
ρ_c (g cm^{-3})	1·20	1·00
ρ_a (g cm^{-3})	1·00	0·001
Non-dimensional parameters		
Fr	–	0·07
$\mathrm{Fr_d}$	0·17	–
Re	20	20
$\mathrm{Re_p}$	0·12	11·0
τ^*_{sa}	–	0·78
τ^*_{sm}	0·61	–

The experiment parameters yield $\mathrm{Fr_d}$ = 0·17 for the submarine cases and Fr = 0·07 for the subaerial cases (Table 3). Both Froude numbers

indicate subcritical flow. For both subaerial and submarine cases, Re = 20, indicating laminar flow. In contrast, natural turbidity currents are turbulent (Heezen & Ewing, 1952; Mulder *et al.*, 1997). Reynolds similarity is a recognized challenge in morphodynamic experiments (Ashmore, 1982; Ashworth *et al.*, 1994; Moreton *et al.*, 2002). However, the patterns of channel and bar formation, which develop through aggradation and shifting of channels, may be relatively insensitive to the presence of turbulence (Malverti *et al.*, 2008; Lajeunesse *et al.*, 2010). The particle Reynolds number is $Re_p = 0{\cdot}12$ for the submarine basin, indicating hydraulically smooth flow conditions. Due to the difference in flow density, $Re_p = 11{\cdot}0$ for subaerial conditions, indicating transitional conditions nearer to hydraulically smooth flow (Nikuradse, 1933).

The above parameters pertain to the initial stages of the experiments, prior to widespread sediment deposition and channel formation. Here, a simple argument based on bed shear stress is used to predict the depth and slope of channels formed during the experiments. For normal flow, the bed shear stresses for subaerial and submarine cases are:

$$\tau_{sa} = \rho g h S \tag{2A}$$

$$\tau_{sm} = (\rho_c - \rho_a) g h S \tag{2B}$$

where the subscripts 'sm' and 'sa' refer to submarine and subaerial cases, respectively; and ρ is the density of water. The relatively low density contrast between the current and the ambient fluid for the submarine case lowers the shear stress; this effect is negligible for the subaerial case (i.e. water flowing beneath air). Equations 2A and 2B imply that to transport the same sediment load, a submarine channel requires a larger depth–slope product compared to a subaerial channel. Konsoer *et al.* (2013) proposed this framework, which is modified by using bulk current density rather than sediment concentration. The predicted ratio of depth-slope product for the submarine versus the subaerial case is:

$$\frac{(hS)_{sm}}{(hS)_{sa}} = \frac{\rho}{\rho_c - \rho_a}. \tag{3}$$

For the experiments, the density in the numerator (ρ) is equal to the density of the ambient fluid in the denominator (ρ_a) and Eq. 3 yields $(hS)_{sm}/(hS)_{sa} = 5{\cdot}0$. Natural submarine channel slopes can be orders of magnitude larger than corresponding river slopes for similar width or depth (Pirmez & Imran, 2003; Konsoer *et al.*, 2013).

The Shields number is:

$$\tau^*_{sa} = \frac{hS}{\left(\frac{\rho_s - \rho}{\rho}\right) D_{50}} \tag{4A}$$

for the subaerial case, where ρ_s is sediment density, and:

$$\tau^*_{sm} = \frac{hS}{\left(\frac{\rho_s - \rho_c}{\rho_c - \rho_a}\right) D_{50}} \tag{4B}$$

for the submarine case. These relations yield $\tau^*_{sm} = 0{\cdot}61$ for the submarine experiments and $\tau^*_{sa} = 0{\cdot}78$ for the subaerial experiments, indicating shear stresses well above the threshold for motion in both cases.

Spatial analysis of bars and channels

Topographic patterns were analysed using two complementary approaches. The first captures topographic variation at the scale of bars and channels and is based on the residual elevation (z_r) after subtracting the large-scale trends in the topography. To calculate z_r, the DEMs were smoothed using a Wiener filter with a 10 × 10 pixel moving window. Longitudinal and transverse trends were removed by subtracting the mean elevation in a square window (100 × 100 pixels). This window is chosen to remove topographic curvature induced by sediment lobes while preserving the signatures of channels and associated bars. This approach, however, is insufficient to fully capture the planform extent of bars and channels, which are intrinsically linked to flow paths. Therefore, a second approach based on reduced-complexity flow modelling was used to map bars and channels as objects.

The geometry of bars and channels in multi-thread channel networks is often mapped manually using inundation (Sapozhnikov & Foufoula-Georgiou, 1996; Cazanacli *et al.*, 2002; Ashworth *et al.*, 2007). A limitation of this technique for experiments is that dye persists in sediments after the cessation of surface flow, which blurs the contrast between channels and their surroundings. As an alternative, a simplified flow

model is used to identify channel networks in topography data. The aim is not to model flow in detail, but rather to use a realistic estimate of inundation to map channels as wetted areas and bars as dry areas. This mapping approach offers several advantages over mapping based on local topographic statistics alone (for example, slope), because the latter cannot account for the connectivity of flow paths that define a complex channel network with both bifurcations and locally adverse slopes (Limaye, 2017).

The chosen flow model, LISFLOOD, is implemented in the CAESAR-LISFLOOD landscape evolution model (Bates *et al.*, 2010; Coulthard *et al.*, 2013; Coulthard, 2017). The model solves a simplified version of the shallow water equations on a rectilinear grid.

The volumetric, modelled discharge between grid cells is:

$$Q_{\mathrm{m}} = \frac{q - gh_{\max}\Delta t \frac{\Delta(h+z)}{\Delta x}}{1 + gh_{\max}\Delta t n^2 |q| / h_{\max}^{10/3}} \Delta x \qquad (5)$$

where q is the width-averaged water flux from one cell to the other, $h_{\max}$ is the maximum flow depth, Δt is the time step, z is elevation, Δx is the grid spacing, and n is Manning's roughness coefficient. The model decomposes flow in the row and column directions, so that the change in flow depth at a cell with row and column coordinates (i, j) is:

$$\frac{\Delta h^{i,j}}{\Delta t} = \frac{Q_x^{i-1,j} - Q_x^{i,j} + Q_y^{i,j-1} - Q_y^{i,j}}{\Delta x^2} \qquad (6)$$

where Q_{x} and Q_{y} are volumetric discharges in the column and row directions, respectively. To balance model run time with grid spacing sufficient to resolve bar and channel structure, the DEMs were resampled from 1 to 10 mm grid spacing for flow modelling.

The following parameters enabled operating the model at experiment scale. Using Manning's equation, n was set to 0·3 to reflect the approximate flow velocity (1 cm s^{-1}), the flow depth of the density currents after sediment deposition and channelization (5 mm), and the main section slope (0·035). This n value is one order of magnitude larger than typical values for open channel flow at natural scale (Chow, 1959), reflecting the laminar flow condition in the channels. During the model runs, a thin layer of flow commonly spread over the low-relief topography in the DEMs. This behaviour occurred for both the subaerial and submarine cases. A threshold flow depth can be applied during the flow routing, but produced a creeping behaviour in the inundation extent. Therefore a vanishingly small depth threshold (10^{-5} m) was applied to the flow model results. This threshold created wetted areas isolated from the channel network, which were removed using a threshold area of 10 pixels.

The DEM was cropped and fitted with synthetic walls at all edges except the downstream edge. Water was introduced to a fictitious reservoir appended to the upstream edge of the DEM, similar to the water reservoir for the line source inlet condition in the experiment (Fig. 2A). The fictitious reservoir spanned the width of the DEM, and a lip was attached to the downstream edge of the reservoir. The lip elevation was constant and equal to the maximum elevation in the first cross-stream column of the original DEM. Upon overtopping the reservoir, flow spilled over this lip, proceeded across the DEM, and concentrated in local topographic lows. After traversing the DEM, flow exited the domain at the downstream edge, where the slope was set to the mean slope of the original DEM.

The topography data was subjected to a gradually increasing modelled discharge from low to high inundation extent. A non-dimensional modelled discharge is defined as:

$$Q_{\mathrm{m}}^{*} = \frac{Q_{\mathrm{m}}}{g^{1/2} L^{5/2}} \qquad (7)$$

where L is a representative length scale defined as the standard deviation of the residual elevation (z_{r}).

For each increment in modelled discharge, discharges entering and leaving the domain equilibrated over 60 min of model time. For each discharge increment, braiding index was measured as the average number of wetted channels in cross-section, following Egozi & Ashmore (2008). Similar to their total braiding index, the mapping does not differentiate threads based on active sediment transport. The mean braiding index includes 10 cross-sections, which were equally spaced (17 cm) in the downstream direction. Bars are defined as dry areas surrounded by wetted areas. The bar aspect ratio is used to quantify bar geometry, and is measured as the ratio of the major and minor axes of a fitted ellipse. As shown below, the map of bars and channels that results from this approach changes with

discharge, as occurs for natural multi-thread channel networks (Mosley, 1982; Robertson-Rintoul & Richards, 1993; Welber *et al.*, 2012). Therefore, for each DEM the inundation map that produced the maximum braiding index was used as the reference map for bar and channel geometry.

Channel avulsions

As shown below, channels formed, migrated, avulsed and aggraded in the experiments. For 20 channels in experiment Submarine 3, which had the longest image time-series (Table 2), the elapsed time was measured starting from the initial, gradual channel motion of the channel to avulsion. Channels were tracked using a distributed sample in the downstream direction and through time. The tracking entailed: (i) identifying active channels by inspecting the images; (ii) following the channels, aided by image software (Asvadi *et al.*, 2014); and (iii) stopping the tracking sequence after an avulsion.

DENSITY CURRENT DYNAMICS

Basin filling

For all submarine experiments, the dense underflow entrained sediment and transported it as bedload across the flume. The deposits accumulated on an initially bare surface. The base case was experiment Submarine 1, which had $Q_w/Q_s = 10$ and a line source inlet condition (Movie S1 in the Supporting Information). Flow channelized near the inlet section, and sediment first accumulated as lobes at the slope break between the inlet section and the main section ($t^* = 0{\cdot}07 \times 10^9$; Fig. 3A), then at the slope break between the main section and end section ($t^* = 0{\cdot}54 \times 10^9$; Fig. 3B). Due to a slight lateral slope in the main section, flow tended to first occupy the downstream-right side of the basin. After sediment filled and levelled this zone, deposition covered the rest of the basin ($t^* = 1{\cdot}65 \times 10^9$; Fig. 3C). Flow transitioned to unchannelized sheet flow and subtle, interwoven channels downstream ($t^* = 1{\cdot}80 \times 10^9$; Fig. 3D). Parts of the surface became morphologically inactive due to channel shifting ($t^* = 1{\cdot}86 \times 10^9$; Fig. 3E).

All of the submarine experiments generated channels. At a larger scale, sediment accumulation patterns varied between experiments. Figure 4 shows examples of these different patterns at the same non-dimensional time as for experiment Submarine 1 in Fig. 3B ($t^* = 0{\cdot}54 \times 10^9$). For experiment Submarine 3 (Fig. 4A), which had a higher flow to sediment

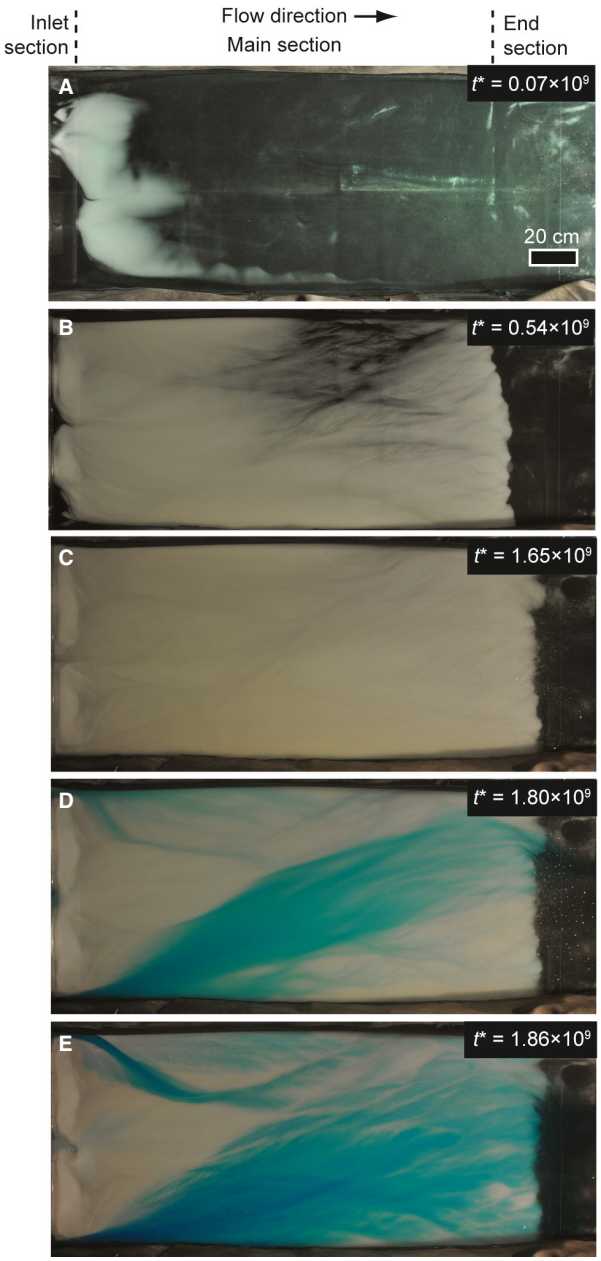

Fig. 3. (A) to (E) A time-series of overhead images looking through the water column for the base case experiment, Submarine 1. See Movie S1 in the Supporting Information for the full duration of the experiment. For all images flow direction is from left to right and the scale is equal. A schematic of the experiment configuration is shown in Fig. 2A. Blue dye in (D) and (E) highlights zones with active and recent saline flow. Time is non-dimensionalized as $t^* = tQ_s/D_{50}{}^3$. (A) $t^* = 0{\cdot}07 \times 10^9$. (B) $t^* = 0{\cdot}54 \times 10^9$. (C) $t^* = 1{\cdot}65 \times 10^9$. (D) $t^* = 1{\cdot}80 \times 10^9$. (E) $t^* = 1{\cdot}86 \times 10^9$.

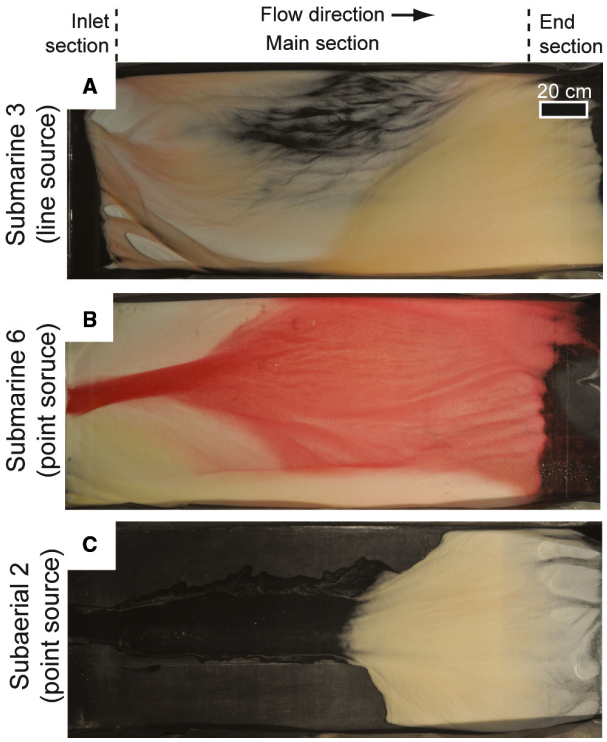

Fig. 4. Overhead images showing different styles of basin-filling for a subset of the experiments. Flow direction is from left to right, and the scale and extent are fixed for all images. Dimensionless time ($t^* = tQ_s/D_{50}^3$) is fixed at $t^* = 0{\cdot}54 \times 10^9$, as in Fig. 3B. The images show experiments (A) Submarine 3, (B) Submarine 6 and (C) Subaerial 2. The sediments are off-white, and the colours correspond to areas with dyed inflow that is either travelling across the basin or is retained in sediment pore space (faint pink in A; red in B).

discharge ratio ($Q_w/Q_s = 27{\cdot}2$) than experiment Submarine 1, sediment advanced further into the basin. For experiment Submarine 6 (Fig. 4B), which had a flow to sediment discharge ratio ($Q_w/Q_s = 10{\cdot}6$) similar to experiment Submarine 1 but a point source inlet condition, a broad sediment fan developed from the inlet and prograded gradually until it spread across the entire main section. For experiment Subaerial 2 (Fig. 4C), which had the same Q_w/Q_s and inlet condition as Submarine 6 but used a subaerial basin condition, a back-stepping fan deposit nucleated from the lower slope break between the main section and the end section. A large proportion of sediment bypassed the main and end sections.

Channel dynamics

Figure 5 shows three example image time-series from the experiment Submarine 3 (Movie S2 in the Supporting Information). Each time-series image uses a separate, fixed observation point and spans a different time interval in the experiment. Figure 5A shows a channel as a distinct red band up to 30 mm across, where the density current is relatively deep and narrow. Twelve minutes later (Δt = 12 min; Fig. 5B), the channel has shifted upward in the image. At Δt = 100 min (Fig. 5C), no channel feature is visible and the saline underflow has shifted elsewhere in the basin. Figure 5D shows a different channel at another time, and with lower colour contrast between the channel and its surroundings. At Δt = 45 min (Fig. 5E), the channel has narrowed and shifted by more than the original channel width towards the lower left corner of the image. At Δt = 40 min (Fig. 5F), the channel has not shifted out of the frame, but instead has been abandoned and is no longer distinctly visible in the image. Figure 5 (panels G to I) shows a similar sequence, this time for a much wider channel *ca* 50 mm across. The three image time series collectively show channels that migrate laterally, change in width, and become abandoned.

Figure 6 shows the distribution of avulsion times for channels in experiment Submarine 3. The modal avulsion time is about 12 min, and progressively fewer channels show longer avulsion times except for three channels at about 50 min. All but one of the channels avulsed in <60 min. The median avulsion time (22 min) is selected as a representative timescale, as discussed below.

TOPOGRAPHIC SIGNATURES OF SUBMARINE BRAIDING

This section compares topographic measures for subaerial and submarine conditions, and for submarine conditions isolates the topographic effects of the ratio of flow to sediment discharge and time.

Topography for submarine versus subaerial conditions

Figure 7 shows shaded relief maps for the base case, which had a line source inlet and a submarine basin condition (Submarine 1; Fig. 7A). Also shown are the other combinations of the inlet condition and the basin condition. Subaerial 1 (Fig. 7B) also used the line source inlet condition while Submarine 6 (Fig. 7C) and Subaerial 2 (Fig. 7D) used the point source inlet

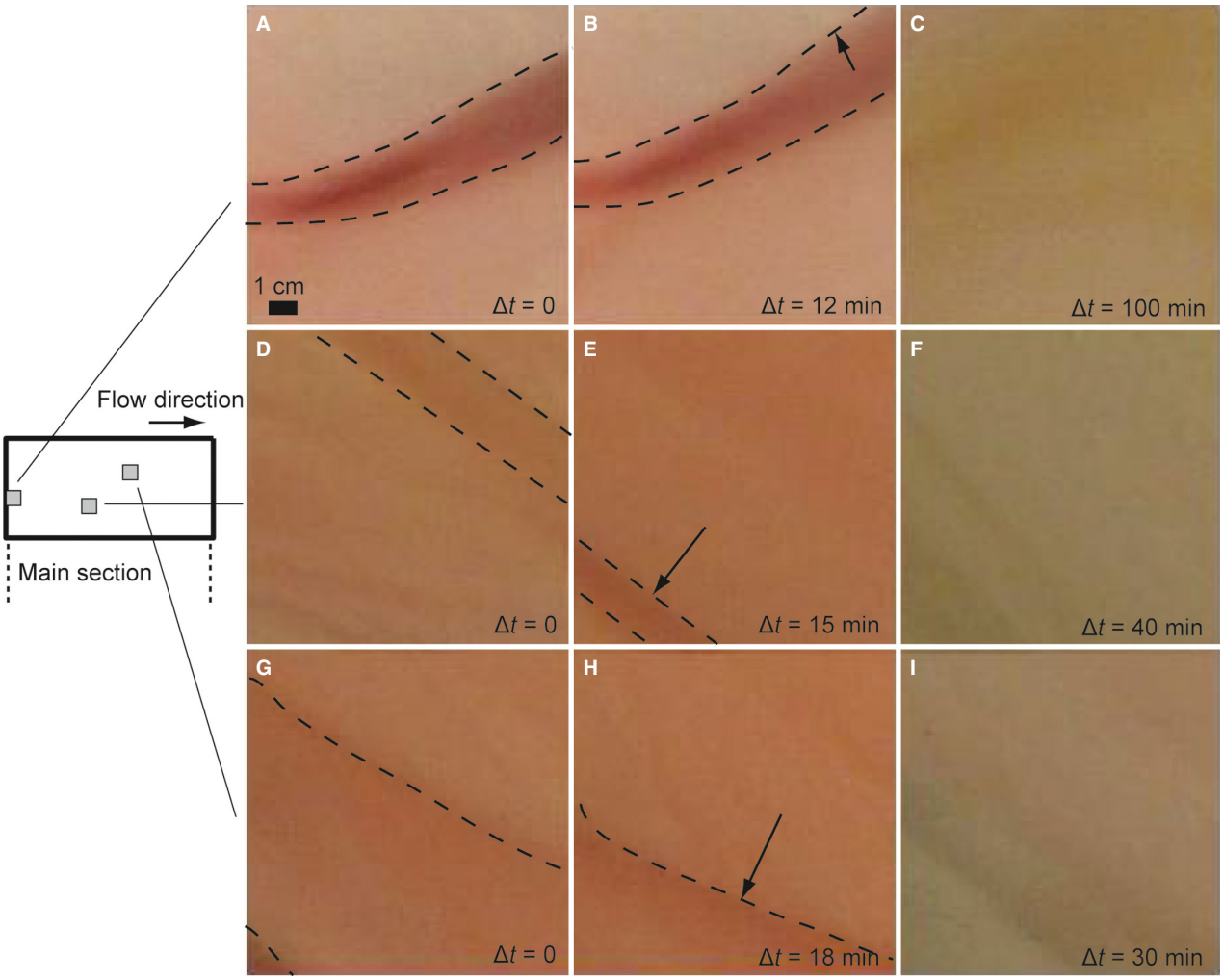

Fig. 5. Images capturing channel migration in experiment Submarine 3. See Movie S2 in the Supporting Information for the full spatial scale and duration of the experiment. Each row represents a time-series of three images for a fixed observation point and shows (from left to right) the channel at an initial time, a later view of the migrated channel, and the view after the channel has been abandoned by avulsion. The time of the initial view and the time interval between images both vary. Dashed lines indicate channel boundaries and arrows indicate channel migration directions. Red dye was intermittently added to the saline underflow and is more intense in zones of higher flow depth. Scale is fixed for all images. Δt indicates the time since the start of each the image time-series. (A) to (C) Migration time-series 1. (D) to (F) Migration time-series 2. (G) to (I) Migration time-series 3.

condition. Data gaps were identified automatically in the DEMs for experiments Submarine 1 and Subaerial 1 and were excluded from the analysis.

The shaded relief map for the base case, Submarine 1 (Fig. 7A), shows subtle bar and channel topography. The shaded relief for Subaerial 1 (Fig. 7B), with the subaerial basin condition, shows more muted channel and bar topography compared to the base case, with few obvious differences in bar and channel dimensions moving downstream. Isolated channels formed by groundwater sapping during pauses in the run. Experiment Submarine 6 (Fig. 7C), with a point source inlet condition, shows a fan-shaped deposit. A single, deep channel upstream transitions to a broad, unchannelized area in the middle of the main section. At the downstream edge, more subtle channels redevelop, similar to the base case. Finally, experiment Subaerial 2 (Fig. 7D) also shows a fan morphology on a large scale, and a dominant channel transitions to more numerous and similarly sized channels downstream. In contrast to the submarine point source case, there is greater fine-scale dissection across the basin.

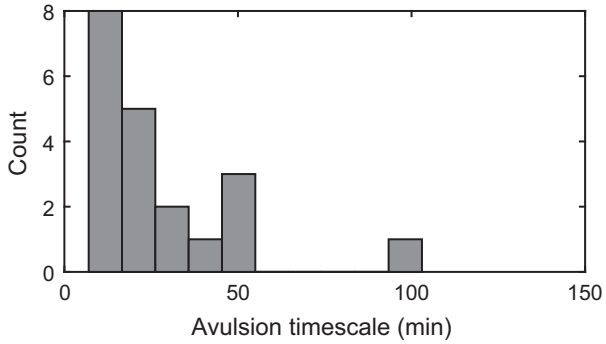

Fig. 6. Histogram of time for avulsion based on 20 observations for experiment Submarine 3.

The dissection, which is subtle in the original DEM, manifests as millimetre-scale deviations from zero in the residual elevation (z_r). Figure 8 shows maps of residual elevation for the same experiments as in Fig. 7. The residual elevation for the submarine base case (Submarine 1; Fig. 8A) shows that channels have negative z_r, while bars and lobes have positive z_r. For experiment Subaerial 1 (Fig. 8B), z_r shows smaller departures from zero compared to the submarine base case. For the submarine case with the point source inlet (Submarine 6; Fig. 8C), the unchannelized zone is clearly visible as an area with near-zero z_r values. The wide channel at the upstream end appears as a zone of strongly negative residual elevation. The subaerial case with the point source inlet (Fig. 8D) shows z_r values at a similar scale compared to the subaerial, line-source inlet case (Fig. 8B), and clearly shows the overall fan morphology. In comparison to the submarine case with the same inlet condition (Fig. 8C), there is no broad zone of near-zero z_r.

The standard deviation of the residual elevation, std(z_r), characterizes topographic variation and serves as a proxy for channel depth. The variation in std(z_r) with downstream distance is considered next, and compared between the submarine and subaerial cases for the same inlet condition. For the line source inlet condition (Fig. 8E), the submarine case shows dramatically higher values of std(z_r) compared to the subaerial case for downstream distances between 0 m and 0·75 m (i.e. about 150 channel depths). Further downstream, the values of std(z_r) overlap and show smaller differences between the subaerial and submarine experiments. For the point-source inlet condition (Fig. 8F), similar trends occur for both the submarine and subaerial cases. After a downstream distance of

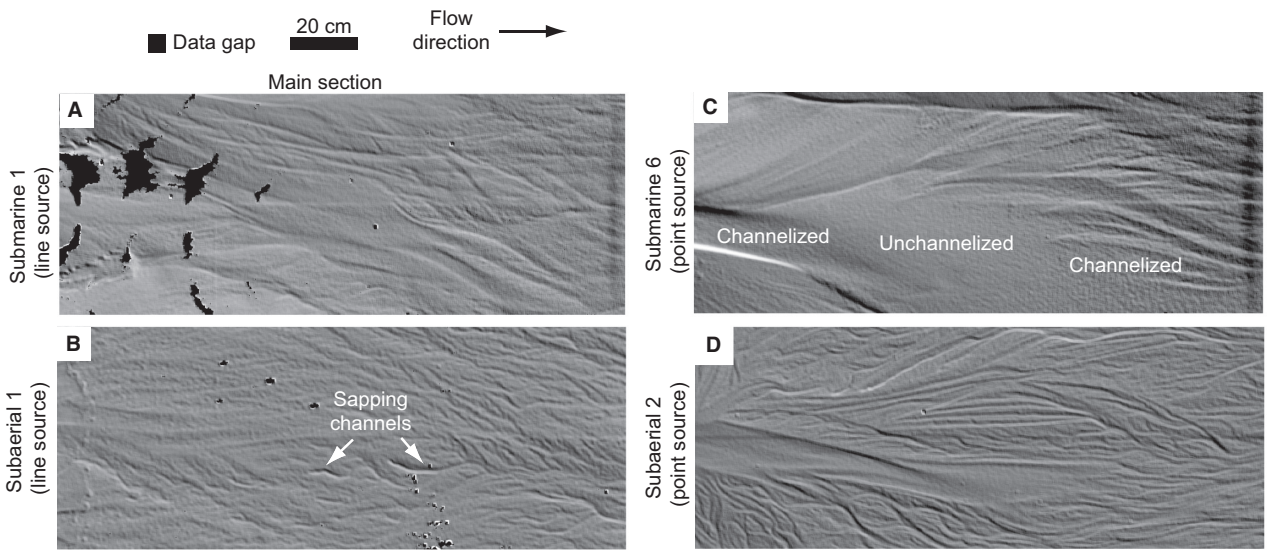

Fig. 7. Shaded relief of final topography for a subset of experiments. Black areas indicate data gaps after artifact removal from the DEMs. For all figures flow direction is from left to right and the scale is constant. Panels (A) and (B) show submarine and subaerial experiments, respectively, for the line source inlet condition and with similar Q_w/Q_s. Panels (C) and (D) show submarine and subaerial experiments, respectively, for the point source inlet condition and with similar Q_w/Q_s. (A) Experiment Submarine 1. (B) Experiment Subaerial 1. Sapping channels that formed during a pause in the experiment are indicated with arrows. (C) Experiment Submarine 6. Channelized and unchannelized areas are labelled. (D) Experiment Subaerial 2. DEM, digital elevation model.

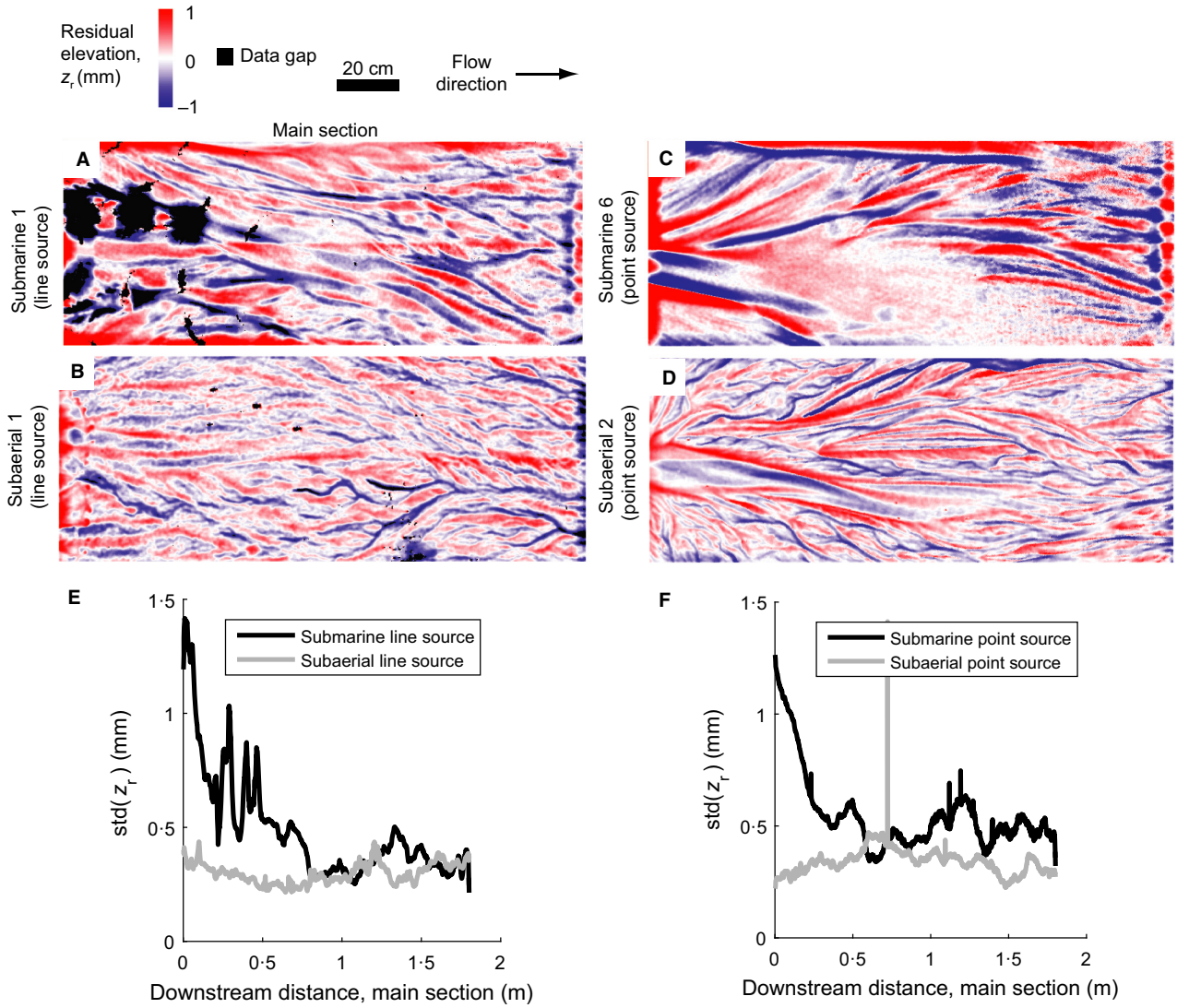

Fig. 8. Maps and spatial statistics of residual elevation, derived by subtracting the moving average elevation in a 100 mm × 100 mm window from the filtered DEM. Maps of residual elevation are based on the final topography for experiments (A) Submarine 1 and (B) Subaerial 1, which used the line source inlet condition and similar values of Q_w/Q_s; and experiments (C) Submarine 6 and (D) Subaerial 2, which used the point source inlet condition and similar Q_w/Q_s. The standard deviation of residual elevation (std(z_r)) versus downstream distance in the main section is plotted for experiments (E) Submarine 1 and Subaerial 1, and (F) Submarine 6 and Subaerial 2. DEM, digital elevation model.

0·5 m (about 100 channel depths), the submarine case shows consistently higher values of std(z_r) compared to the subaerial case, although these are still smaller than for the submarine case upstream of 0·5 m.

Figure 9 shows cross-stream averaged elevation and slope profiles, for the same set of experiments as in Figs 7 and 8. For the line source inlet condition, the longitudinal profile (Fig. 9A) is steeper for the submarine case than the subaerial case. The slope profiles (Fig. 9B) both show overall decreasing slopes in the downstream direction, but the submarine case shows a larger decrease. The point source inlet condition shows similar overall trends in elevation (Fig. 9C) and slope (Fig. 9D) profiles, but with a larger difference in slope between the submarine and subaerial cases.

The preceding analysis yields downstream trends in slope (Fig. 9B and D) and std(z_r) (Fig. 8E and F), a proxy for channel depth (h_p). In Fig. 10, these data are used to estimate the ratio of the depth–slope product for submarine versus subaerial conditions, and to test the

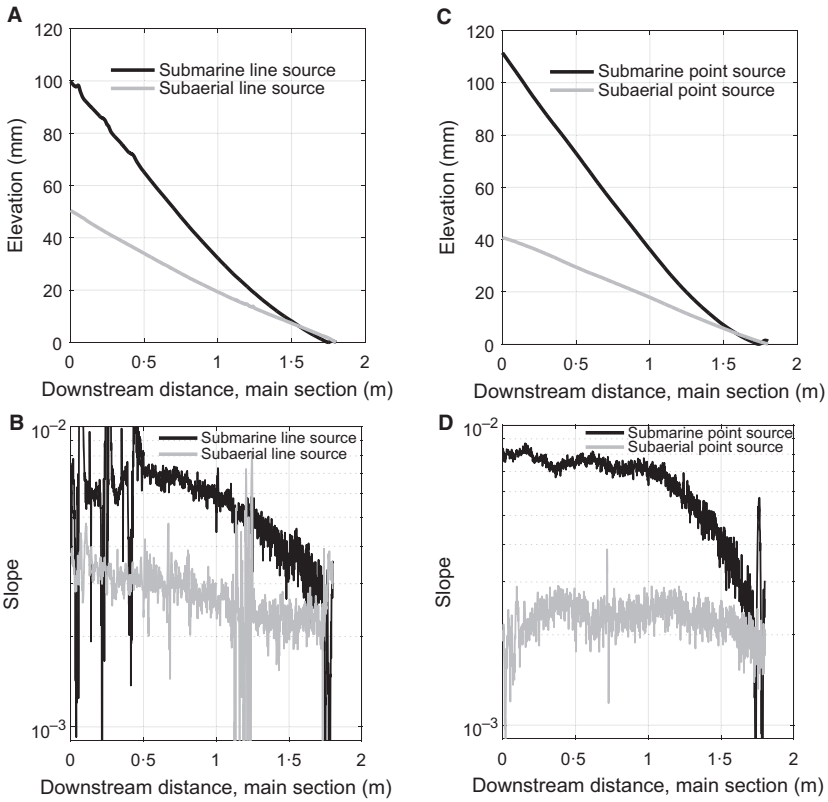

Fig. 9. Downstream elevation and slope profiles for submarine versus subaerial experiments. Elevation is averaged in the cross-stream direction. Slope is the absolute value of the downstream gradient in the averaged elevation profile. (A) Elevation and (B) slope versus downstream distance for submarine and subaerial experiments, respectively, for the line source inlet condition and with similar Q_w/Q_s (experiments Submarine 1 and Subaerial 1). (C) Elevation and (D) slope versus downstream distance for submarine and subaerial experiments, respectively, for the point source inlet condition and with similar Q_w/Q_s (experiments Submarine 6 and Subaerial 2).

theoretical prediction from Eq. 3. Assuming that this scaling between std(z_r) and channel depth is consistent between subaerial and submarine cases, the ratio $(h_pS)_{sm}/(h_pS)_{sa}$ represents the actual ratio of depth-slope product for the submarine versus the subaerial cases. These calculations use the experiments with $Q_w/Q_s \approx 10$, and separately compare submarine and subaerial topography for the line source inlet condition (experiments Submarine 1 and Subaerial 1) and the point source inlet condition (experiments Submarine 6 and Subaerial 2).

For the line source inlet condition, $(h_pS)_{sm}/(h_pS)_{sa}$ varies between 3 and 10 for downstream distances up to 0·6 m, and therefore encompasses the predicted ratio of 5·0. For greater downstream distances, $(h_pS)_{sm}/(h_pS)_{sa}$ declines to roughly half the predicted value. For the point source inlet condition, the ratio begins at 27, and then declines rapidly with downstream distance and approaches the predicted ratio ($(h_pS)_{sm}/(h_pS)_{sa} = 5$) near a downstream distance of 0·3 m (about 60 channel depths). Further downstream, the $(h_pS)_{sm}/(h_pS)_{sa}$ ratio varies between 2 and 5 and, like the line-source case, is lower than the predicted value. Both the line-source and point-source experiments indicate that the depth-slope product is generally larger for the submarine basin than for the subaerial basin, and arises due to roughly equal increases in both channel depth (Fig. 8) and slope (Fig. 9) for the submarine basin.

Effects of flow to sediment discharge ratio

Figure 11 shows the downstream trends in topography for different values of flow to sediment discharge ratio (Q_w/Q_s), and for both the line-source (Fig. 11A to C) and point-source (Fig. 11D to F) inlet conditions. For the line source for each of three different discharges (Fig. 11A), std(z_r) varies widely for downstream distances <0·5 m. Downstream of 0·5 m, the case with $Q_w/Q_s = 27·2$ shows substantially higher values of std(z_r) compared with the other two cases with lower Q_w/Q_s values, which show similar values of std(z_r). The longitudinal profiles for the same three experiments all show overall concave shapes (Fig. 11B). The slope profiles (Fig. 11C) further show that all three surface profiles are slightly convex until 0·5 m downstream.

Two values of Q_w/Q_s were tested for the point-source inlet condition. The case with $Q_w/$

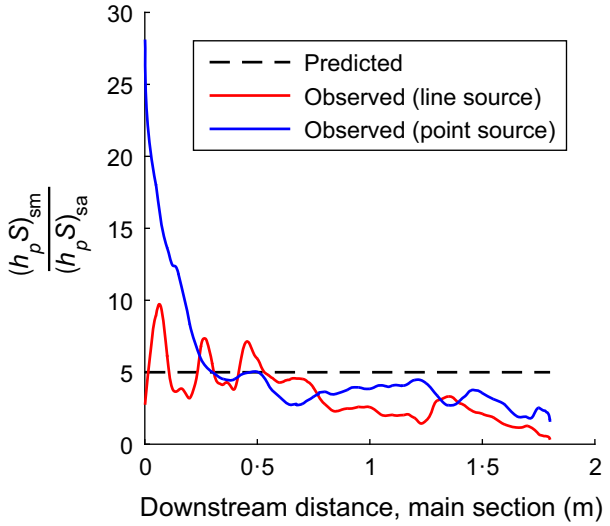

Fig. 10. The ratio of the estimated depth-slope product for submarine versus subaerial conditions, plotted versus downstream distance. The standard deviation of residual elevation in the cross-stream direction, std(z_r), is used as a proxy for channel depth (h_p). Separate curves are shown for the line source inlet condition (red; experiments Submarine 1 and Subaerial 1) and the point source inlet condition (blue; experiments Submarine 6 and Subaerial 2). The dashed black line indicates the predicted ratio of depth-slope product from Eq. 3.

Q_s = 10·0 shows substantially higher values of std(z_r) near the inlet (Fig. 11D) than the case with Q_w/Q_s = 18·6. The curves occupy a similar range between 0·5 m and 1·0 m downstream, and then the case with Q_w/Q_s = 10·0 again shows higher values of std(z_r). The longitudinal profiles (Fig. 11E) and slopes (Fig. 11F) for the point source experiments show a transition from linear to concave slopes downstream. The experiment with Q_w/Q_s = 10·0 has a higher slope than the experiment Q_w/Q_s = 18·6, except between 0·4 m and 0·8 m downstream, where the slopes overlap.

Bar and channel geometry

As discussed above, a reduced-complexity flow model is used to map flow paths and delineate bars and channels (Limaye, 2017). Figure 12 shows an example of this approach for the topography of experiment Subaerial 1, which is subjected to three modelled discharges of increasing magnitude. For the lowest modelled discharge (Q^*_m = 0·09; Fig. 12A), several channel threads emanate from the inlet. The threads bifurcate downstream, and then coalesce near the end of the domain. Large areas of the domain are not bounded by wetted areas, and therefore show no structure in the inundation map. For Q^*_m = 0·62 (Fig. 12B), the higher modelled discharge causes a larger inundated area and reveals more channels. Similar behaviour occurs for a further increase in Q^*_m (Q^*_m = 80·06; Fig. 12C).

Figure 12D shows the number of bars versus Q^*_m. The first bars are mapped just below Q^*_m = 1, and bars become more numerous with increasing discharge. The number of bars reaches a maximum at Q^*_m = 10, and then declines; neither the rising nor the falling limb in the number of bars is strictly monotonic. The mean braiding index (Fig. 12E) shows the same general relationship to Q^*_m, but peaks near Q^*_m = 1. For a given DEM, the bar and channel map corresponding to the peak mean braiding index was chosen as the representative bar and channel map.

Following this example, the braiding index for the representative bar and channel map was calculated for several DEMs. Figure 13 plots braiding index versus downstream distance; Fig. 13A and B isolate the effect of basin condition, with other factors fixed. In Fig. 13A, the experiments represent the point source inlet condition for subaerial and submarine conditions. The braiding index varies between 6 and 12 for the subaerial experiment, and between 3 and 6 for the submarine experiment. The mean of all the measurements is 8·5 for the subaerial case compared to 5·0 for the submarine case. Figure 13B also compares subaerial and submarine experiments, but for the point-source inlet condition. The braiding index varies more widely than for the line source inlet condition: from 4 to 12 for the subaerial case, and from 4 to 10 for the submarine case. As for the line source experiments, the mean braiding index for the subaerial case (7·5) is higher than for the submarine case (6·0).

Figure 13 (panels C and D) isolates the effect of differences in water discharge in the submarine experiments, with other factors fixed. In Fig. 13C, the experiments represent the line source inlet condition for two experiments with the same sediment discharge but different values of water discharge (Q_w = 0·046 L s^{-1} and 0·0625 L s^{-1}). For both cases, the braiding index varies over a similar range. The mean braiding index is somewhat higher for the lower discharge (Q_w = 0·0046 L s^{-1}). Figure 13D also compares experiments with the same sediment

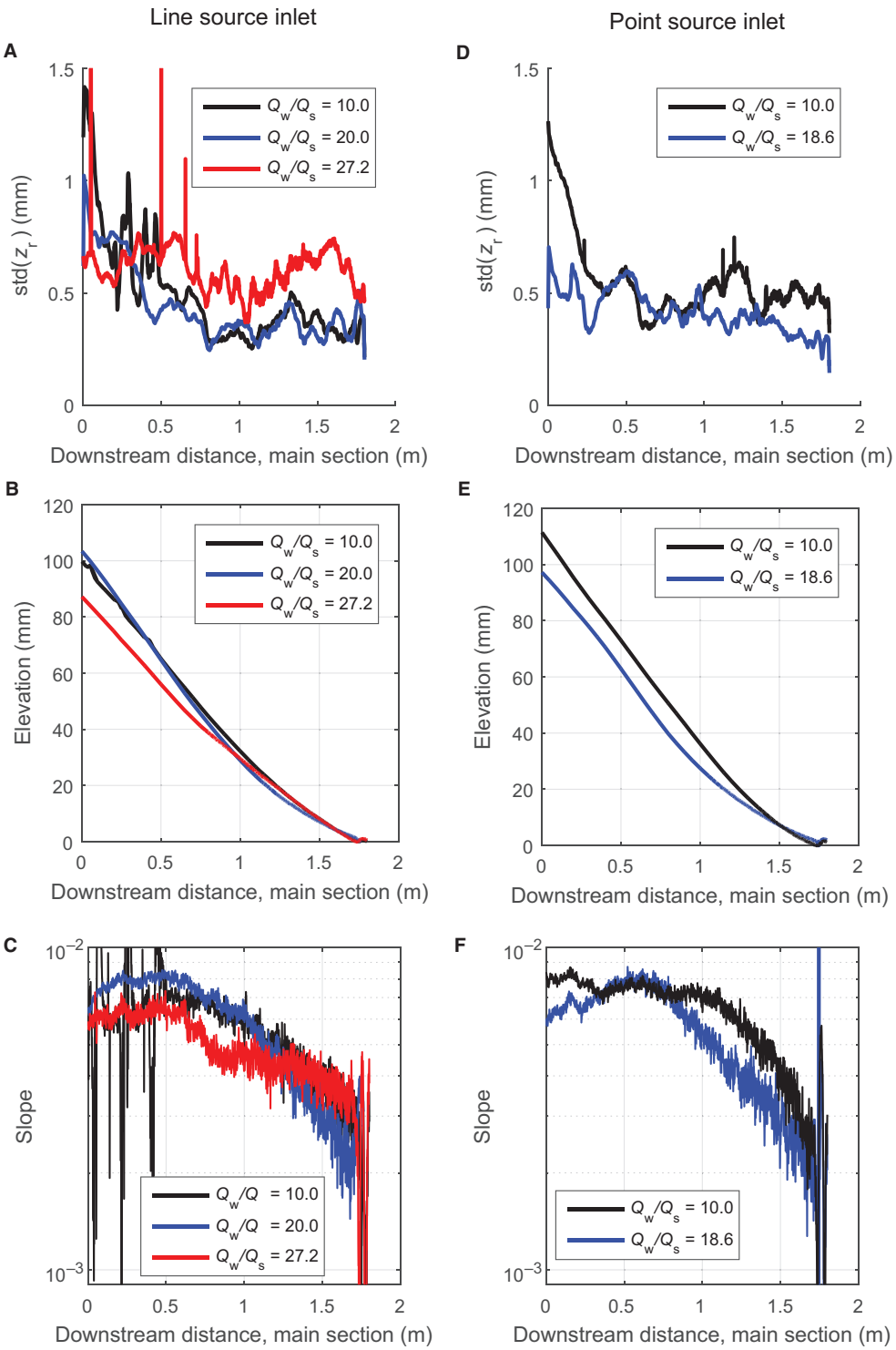

Fig. 11. Downstream trends in topography for different Q_w/Q_s. Panels (A) to (C) correspond to the line source inlet condition. Panels (D) to (F) correspond to the point source inlet condition. Averaged elevation and slope profiles are calculated as in Fig. 9. (A) The standard deviation of residual elevation in the cross-stream direction, std (z_r), for Q_w/Q_s = 10·0 (black; experiment Submarine 1), Q_w/Q_s = 20·0 (blue; experiment Submarine 2), and Q_w/Q_s = 27·2 (red; experiment Submarine 3). (B) Averaged elevation and (C) slope, for the same experiments. (D) The std(z_r) for Q_w/Q_s = 10·0 (black; experiment Submarine 6), Q_w/Q_s = 18·6 (blue; experiment Submarine 5). (E) Averaged elevation and (F) slope, for the same experiments.

discharges but different water discharges (Q_w = 0·035 L s^{-1} and 0·065 L s^{-1}), and for the point source inlet condition. For this comparison, the lower-discharge and higher-discharge cases show identical values of mean braiding index (6·0).

Figure 14 shows the mean bar aspect ratio (i.e. length divided by width), for the representative bar and channel map for the last DEM for each experiment, versus downstream distance. Figure 14A compares submarine and subaerial experiments for the point source inlet condition. The number of bars is higher in the subaerial case, consistent with the higher braiding index (Fig. 13A). The mean bar aspect ratio is nearly identical for both the subaerial and submarine cases. The experiments with the point source inlet condition (Fig. 14B) show similar behaviour in the number of bars, but a larger difference in the mean bar aspect ratio between the subaerial and submarine cases.

As in Fig. 13C, for Fig. 14C the experiments represent the line source inlet condition for two experiments with the same sediment

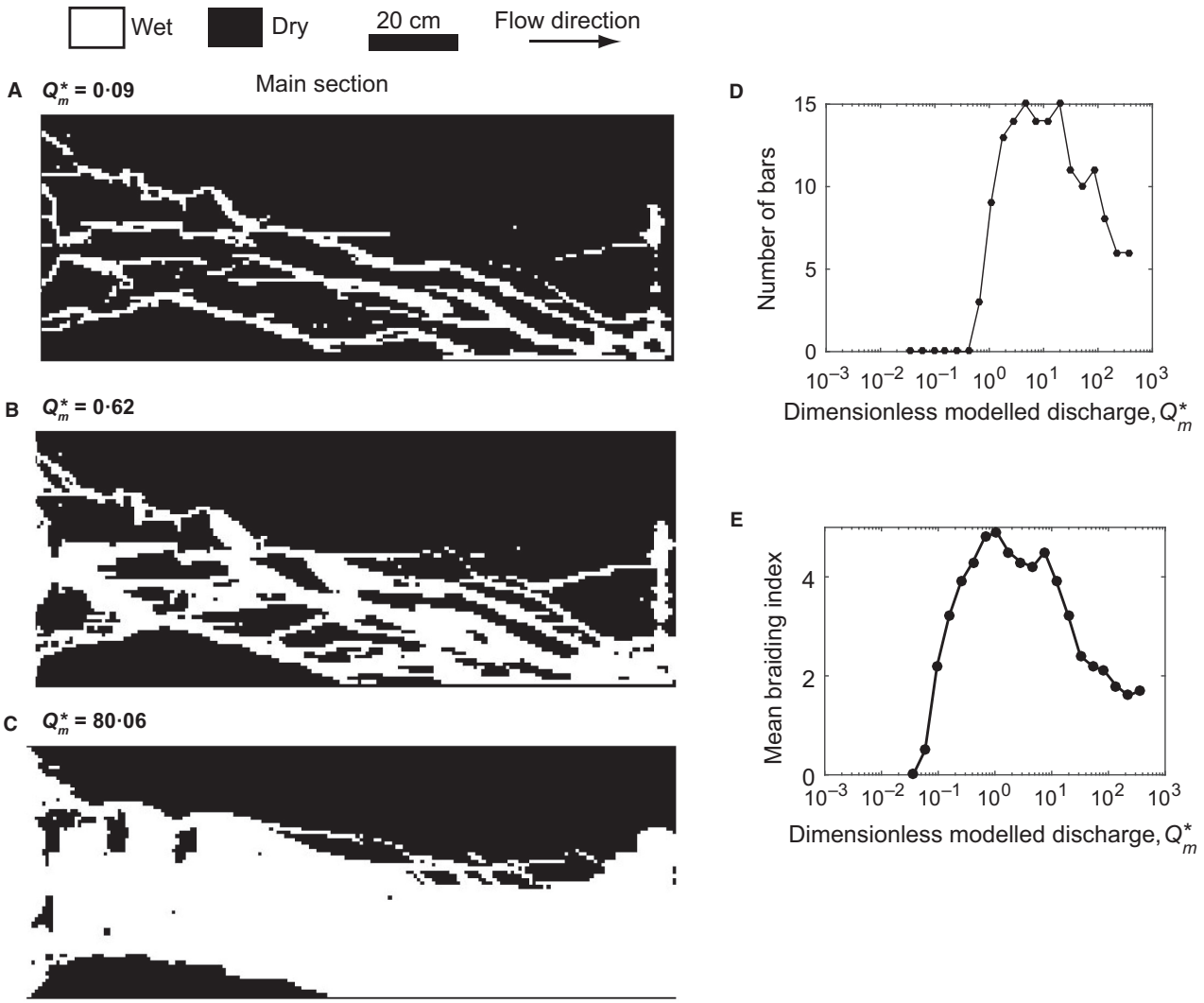

Fig. 12. Maps and statistics of bars and channels, based on reduced-complexity flow modelling. Using a range of discharge, the model was applied to the final topography for experiment Submarine 1. Inundated areas are mapped in white and classified as channels. Dry areas are mapped in black and classified as bars. The distinction between wet and dry areas uses a fixed flow depth threshold of 0·01 mm. Modelled discharge (Q_m) is non-dimensionalized as $Q_m^* = Q_m/(g^{1/2}L^{5/2})$, where L is the standard deviation of the residual elevation for the full domain. For all figures the scale is constant and the modelled flow direction is left to right, consistent with the actual flow direction. (A) Q_m^* = 0·09. (B) Q_m^* = 0·62. (C) Q_m^* = 80·06. (D) Number of bars versus Q_m^*. (E) Mean braiding index versus Q_m^*.

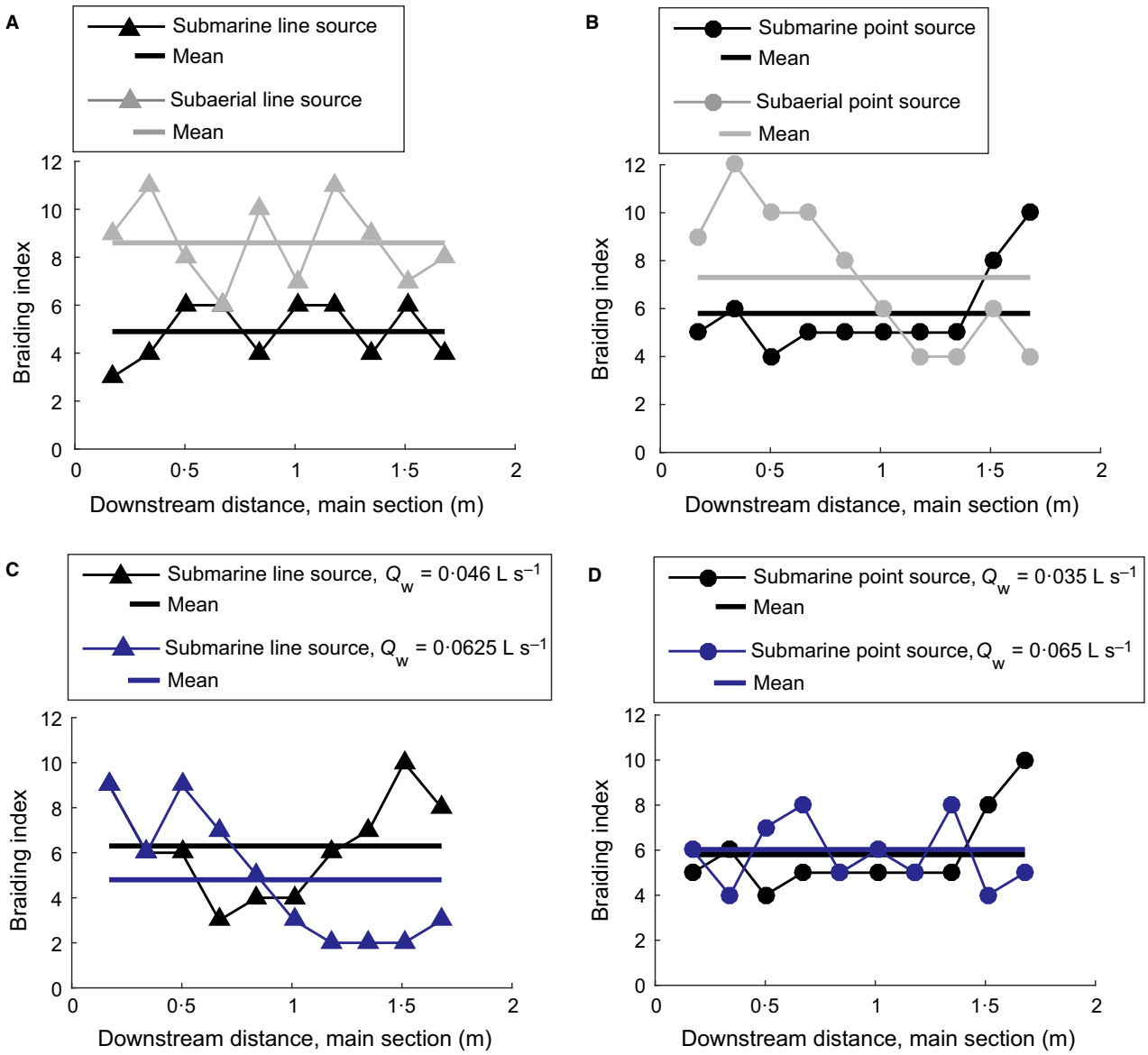

Fig. 13. Braiding index versus downstream distance. The mean braiding index is indicated by a thick line in each plot. (A) Braiding index for submarine and subaerial conditions, with the line source inlet (experiments Submarine 1 and Subaerial 1); and (B) submarine and subaerial conditions, with the point source inlet (experiments Submarine 6 and Subaerial 2). (C) Braiding index for two values of water discharge (Q_w), with sediment flux fixed and the line source inlet condition (experiments Submarine 2 and Submarine 3). (D) Braiding index for two values of water discharge (Q_w), with sediment flux fixed and the point source inlet condition (experiments Submarine 5 and Submarine 6).

discharge but different values of water discharge (Q_w = 0·046 L s^{-1} and 0·0625 L s^{-1}). Fewer bars occur for the case with Q_w = 0·0625 L s^{-1}, and no bars occur downstream of 1·0 m. The mean bar aspect ratio, however, is nearly identical between the two cases. For the point source inlet condition (Fig. 14D), the bars are more numerous and spatially distributed for the higher-discharge case (Q_w = 0·065 L s^{-1}). As for the line-source inlet condition, only a minor difference in the mean bar aspect ratio occurs with the change in Q_w.

In summary, the channel and bar measurements indicate higher values of braiding index for subaerial versus submarine experiments, with other factors fixed. Bars are correspondingly more numerous in the subaerial case, and

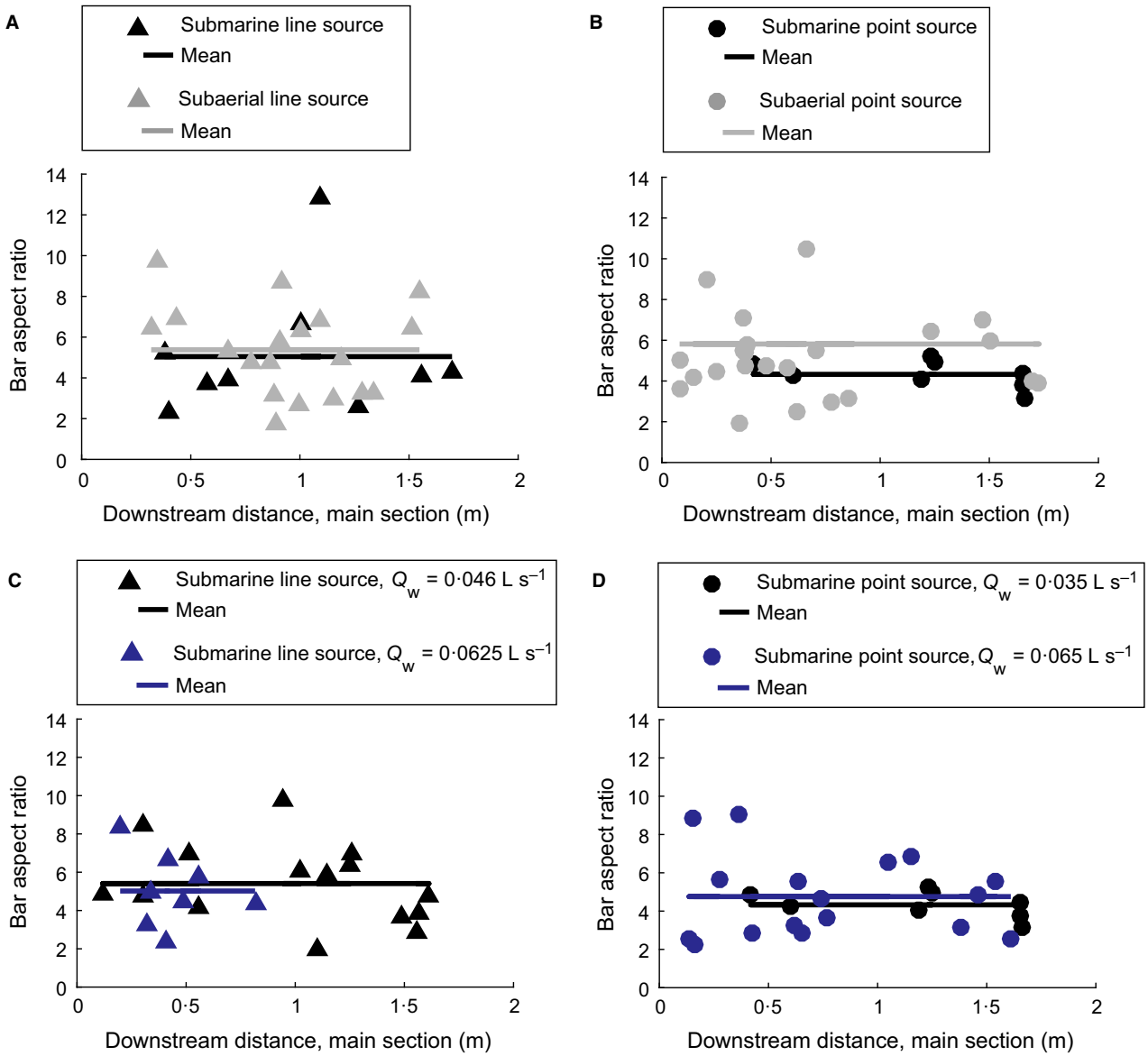

Fig. 14. Bar aspect ratio versus downstream distance. The mean bar aspect ratio is indicated in each plot. The experiments for each plot correspond to those in the corresponding subfigure of Fig. 13. (A) Bar aspect ratio for submarine and subaerial conditions, with the line source inlet; and (B) submarine and subaerial conditions, with the point source inlet. (C) Bar aspect ratio for two values of water discharge (Q_w) with sediment flux fixed and the line source inlet condition. (D) Braiding index for two values of water discharge (Q_w) with sediment flux fixed and the point source inlet condition.

show higher average bar aspect ratios for one of the inlet conditions. For a fixed sediment discharge, the submarine experiments do not show systematic changes in either braiding index or bar aspect ratio for increasing flow discharge.

Time evolution

The analysis turns next to the time evolution of the topography, channel and bar measures. As for the previous image analysis, the topography time-series analysis focuses on experiment Submarine 3. The analysis is limited to the DEMs acquired while the main section was covered with sediment.

The standard deviation of the residual elevation, calculated for the entire residual DEM, varied by about 20% with time (Fig. 15A). Figure 15B shows the mean elevation profile versus downstream distance and through time. The

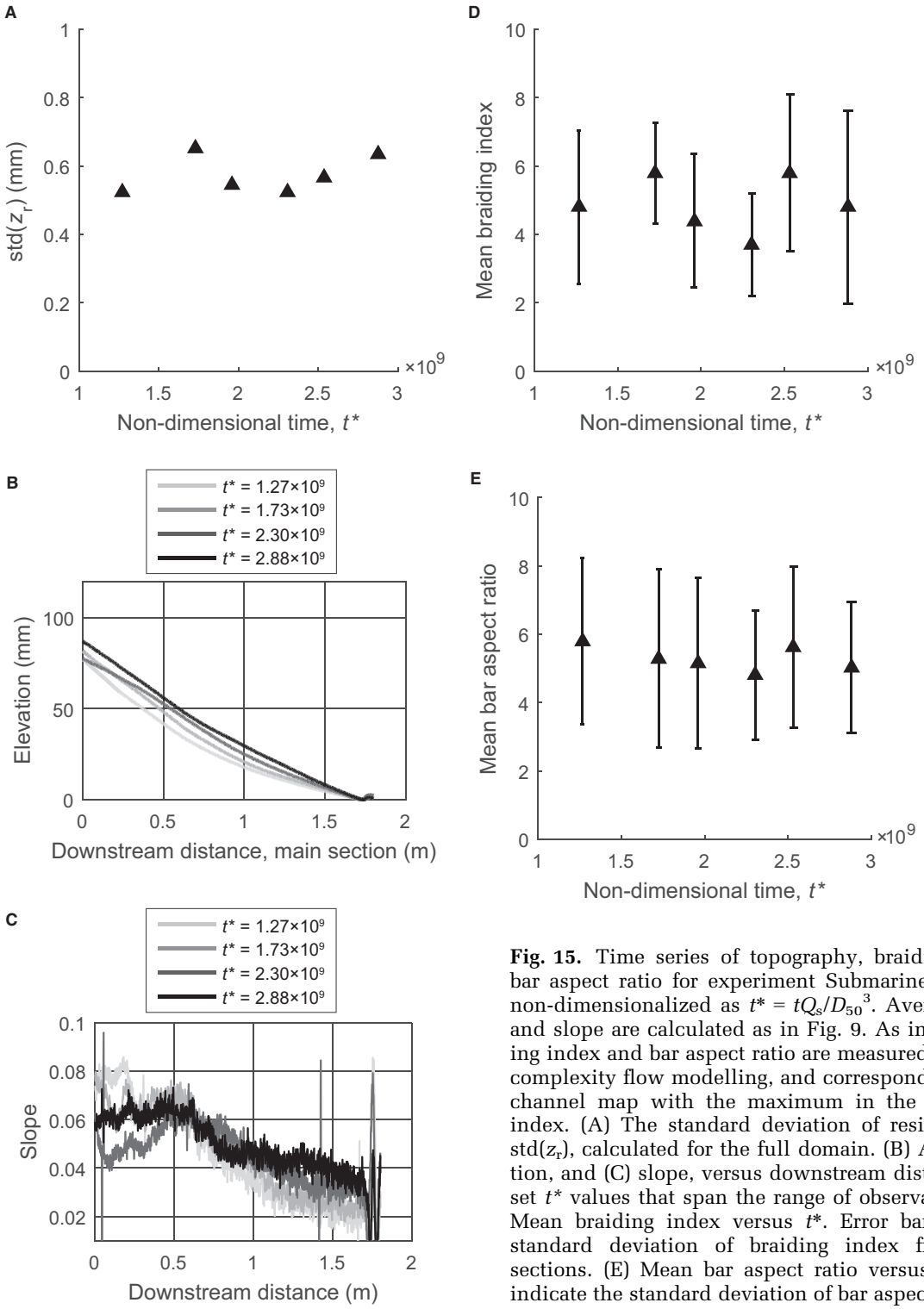

Fig. 15. Time series of topography, braiding index, and bar aspect ratio for experiment Submarine 3. Time (t) is non-dimensionalized as $t^* = tQ_s/D_{50}^3$. Averaged elevation and slope are calculated as in Fig. 9. As in Fig. 12, braiding index and bar aspect ratio are measured from reduced-complexity flow modelling, and correspond to the bar and channel map with the maximum in the mean braiding index. (A) The standard deviation of residual elevation, std(z_r), calculated for the full domain. (B) Averaged elevation, and (C) slope, versus downstream distance for a subset t^* values that span the range of observation times. (D) Mean braiding index versus t^*. Error bars indicate the standard deviation of braiding index from 10 cross-sections. (E) Mean bar aspect ratio versus t^*. Error bars indicate the standard deviation of bar aspect ratio.

longitudinal profile evolved through much of the experiment, and decreased in concavity overall. The time series of slope versus downstream distance (Fig. 15C) shows alternating decreases and increases in slope upstream of 1 m. Downstream of 1 m, the overall slope increased with time. Figure 15 (panels D and E) shows the time evolution of mean braiding index and mean bar aspect ratio, respectively. Both measures vary by about 20%, and neither shows a consistent trend in time.

STRATIGRAPHIC MODEL

The preceding analyses of image and topography data inform a stratigraphic model for aggrading submarine channels. The model is based on characteristic timescales for channel motion that set the geometry of channel sand bodies, as proposed by Jerolmack & Mohrig (2007): the avulsion timescale (t_{av}), the timescale of gradual channel migration by one channel width (t_m) and the timescale for aggradation by one channel depth (t_{ag}). Both channel width and the rate of gradual channel migration varied widely in space and time during the experiments (for example, Fig. 5D and E). These dynamics are characteristic of braided rivers (Ashmore, 2013) and complicate direct measurements of channel migration rates. Based on images (for example, Fig. 5), t_m was estimated as 10 min. This timescale is shorter than the interval between topographic scans. Therefore, the mean channel aggradation rate was calculated based on the total accumulated sediment volume in the main section and the total experiment time. For experiment Submarine 3, this calculation implied a mean channel aggradation rate of 5 mm h^{-1}. Using a channel depth of 5 mm, this rate implies t_{ag} = 60 min.

The estimated timescales for channel motion were combined to generate the stratigraphic model (Fig. 16). First, the timescales for channel motion were related to t_{av}, yielding $t_m \approx 0{\cdot}5t_{av}$ and $t_{ag} \approx 3t_{av}$. For simplicity, in the model the channel width and depth are fixed, the channels only aggrade, and fine sediment is assumed to accumulate outside channels to match channel aggradation (e.g. Jerolmack & Paola, 2007; Fig. 16A).

Figure 16B shows one realization of this model, along a cross-section oriented perpendicular to the mean flow direction. Each channel body represents the lateral and vertical motion of one channel between avulsions. For example, Channel Body 1 formed by migration of a channel to the right. The width of the channel body is limited by the maximum lateral channel displacement: the product of the avulsion timescale and the channel lateral migration rate, for unidirectional channel migration. Including the initial channel position, this maximum channel body

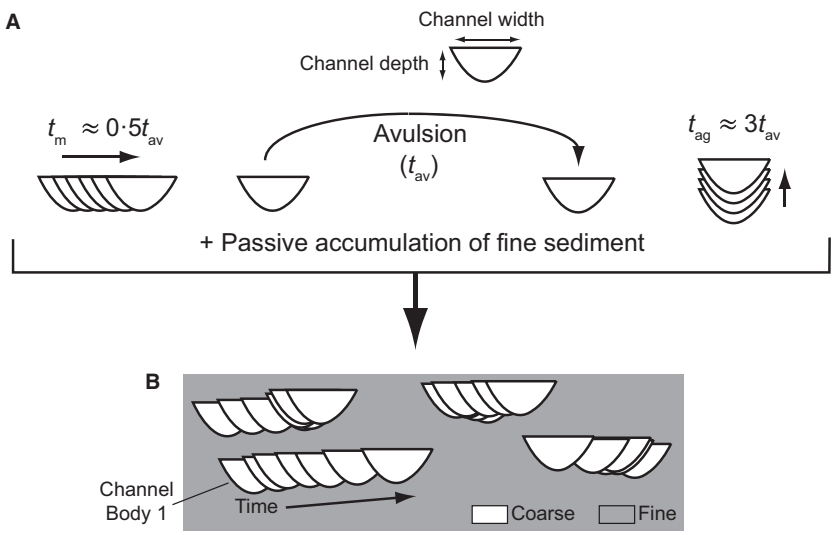

Fig. 16. Schematic reservoir model for braided submarine channels. (A) The model components, including lateral channel migration, avulsion, aggradation and passive accumulation of fine sediment in unchannelized areas. The channel avulsion timescale (t_{av}), aggradation timescale (t_{ag}), and lateral migration timescale (t_m) are based on observations for experiment Submarine 3. These relative timescales inform (B) the stratigraphic model, which represents a cross-section parallel to the mean flow direction. Coarse sediments occupy channel fills (white) in a matrix of fine sediments (grey).

width is three channel widths. The stratigraphic relief of the channel body is approximately one-third of the channel depth, which is the channel aggradation rate multiplied by the avulsion timescale. At each avulsion, a new channel body is generated by shifting the channel laterally over an arbitrary distance. Then the same timescales of channel motion were imposed, but the direction of lateral channel migration was varied, creating different channel trajectories and channel-body shapes.

DISCUSSION

The experiments developed subaqueous braided channels by sediment deposition, consistent with several recent experiments (Métivier *et al.*, 2005; Yu *et al.*, 2006; Rowland *et al.*, 2010; Foreman *et al.*, 2015; Lai *et al.*, 2017). The experiments yielded three previously undocumented phenomena for submarine channels: (i) spatial transitions between channelized flow and sheet flow (Fig. 7C); (ii) downstream decreases in a proxy for channel depth (Fig. 8E and F); and (iii) channelization at the toe of the deposit (Fig. 7A and C), where models often predict unchannelized lobes (Normark, 1970; Walker, 1978; Prélat *et al.*, 2010). The origin of this distal channelization is uncertain, but is most likely to be related to flow drawdown due to the deep sump in the basin (Fig. 2A). The downstream decrease in channel depth for the submarine cases is consistent with observations for natural submarine fans (Flood & Damuth, 1987; Pirmez & Imran, 2003).

Among the independent variables in the experiments – including dimensionless flow discharge (Q^*), the ratio of flow to sediment discharge (Q_w/Q_s), dimensionless time (t^*) and the inlet condition – the clearest controlling factor for topography is whether the basin is subaerial or submarine. For submarine conditions the topography is more exaggerated (Fig. 8), steeper (Fig. 9) and includes fewer channels (Figs 8, 13A and 13B) compared to subaerial conditions. The higher channel slopes are consistent with observations for natural submarine channels (Konsoer *et al.*, 2013), and the coupled increases in topographic variation and slope are consistent with a theoretical prediction of channel geometry based on the density contrast between the current and the ambient fluid (Eq. 3). Importantly, the experiments suggest that the higher depth-slope product for the submarine channels is driven by increases in both channel depth and slope, and that both factors can inform hydraulic reconstruction for turbidity currents (e.g. Pirmez & Imran, 2003). The largest departure between the predicted and observed depth-slope product for the submarine versus the subaerial case occurred near the inlet, where flow is unsteady (Fig. 10).

For steady-state alluvial topography, higher ratios of flow to sediment discharge (Q_w/Q_s) yield lower slopes (Paola *et al.*, 1992). In contrast, in the experiments, slope was locally higher for experiments with higher values of Q_w/Q_s (Fig. 11C and F). This discrepancy suggests that, in general, the experiments did not reach topographic steady state (Fig. 15B and C). Longer run times would require modifying the experiment design [for example, with a rising inlet that overcomes sediment back-filling (Ashworth *et al.*, 2007)].

In previous experiments, the braiding index for subaerial (Bertoldi *et al.*, 2009; Egozi & Ashmore, 2009) and submarine braided channels (Lai *et al.*, 2017) correlated with stream power, which is proportional to inflow discharge. In contrast, the present experiments indicated no such relationship (Fig. 13C and D). Three factors may explain this discrepancy. First, the development of sheet flow in the submarine experiments probably disrupts the link between inflow discharge and the number of channels. Second, the braiding index was measured from topography, whereas the previous studies used images. Third, the baseline for the measurements – the length to width ratio of the experimental basin – was shorter (1·7) than for previous subaerial experiments [6·0 for Egozi & Ashmore (2009); 8·6 for Bertoldi *et al.* (2009)].

Channel networks have been previously mapped for convergent topography using flow models driven by surface slopes alone. This approach has standardized analyses between experiments, numerical models and field data across a scale range of $>10^6$ (Braun & Sambridge, 1997; Tarboton, 1997; Lague *et al.*, 2003; Passalacqua *et al.*, 2010). To the authors' knowledge, this study represents the first application of a reduced-complexity flow model to topographic analysis for experimental channel networks that include bifurcations.

The dimensions of sand bodies emplaced by meandering channels differ strongly between subaerial and submarine cases (Jobe *et al.*, 2016), but this distinction may not hold for braided channels. The kinematics of the experimental density currents imply stratigraphy with low vertical persistence of channel bodies,

similar to natural braided rivers (Fig. 16; Bridge & Lunt, 2006). Fine sediments may also steer submarine channel trajectories through bank strength effects and levée confinement (Peakall *et al.*, 2000; Straub & Mohrig, 2008; Jobe *et al.*, 2016). An important target for future experiments is to test whether fines alter channel trajectories. If they do not, submarine braided channels may reflect coarse-sediment dynamics obscured in single-thread channels.

The emerging picture of submarine braiding partially resembles subaerial braiding. For the submarine experiments, the basin-averaged flow width (1 m) and depth (<10 mm) imply a width to depth ratio >100. Braiding under this geometry is consistent with rivers (Parker, 1976; Foreman *et al.*, 2015; Lai *et al.*, 2017). Experiments further show that similarly to braided rivers, submarine braided channels can develop under constant inflow discharge and with limited confinement and bank cohesion.

Submarine and subaerial braiding also differ in several ways. Beyond the aforementioned geometric differences, for submarine channels, bars are not tall enough to subdivide flow into multiple threads, as occurs in braided rivers (Wynn *et al.*, 2007; Foreman *et al.*, 2015). In the experiments, laminar flow prevents the flow surface from fluctuating upward, as occurs in natural turbidity currents, and therefore restricts flow depths and favours flow division. Experimental and natural density currents show velocity profiles similar to wall-bounded jets (Kneller & Buckee, 2000; Xu, 2010), which differ from rivers and may account for further geometric differences. Moreover, sediment calibre probably differs between the subaerial and submarine environments. In submarine channels, most sediment derives indirectly or directly from the lower reaches of rivers, which generally have fine grain sizes (Romans *et al.*, 2009; Sømme *et al.*, 2009). The occurrence of braiding on some low-latitude submarine fans without direct sources of coarse sediment suggests that other factors – perhaps including remobilization of sediments on continental shelves (Covault & Graham, 2010) or sharp decreases in sediment transport capacity driven by bathymetry (Wynn *et al.*, 2007) – facilitate braiding.

CONCLUSIONS

A series of eight experiments that generated braided channels and bars, including six under subaqueous conditions and two under subaerial conditions, show that:

1 Compared with the subaerial experiments conducted under similar conditions, the subaqueous experiments developed fewer channels, deeper channels near the inlet and progressively smaller variations in topography with distance downstream.

2 The ratio of the depth-slope product for submarine versus subaerial conditions was always greater than unity and overall consistent with the predicted ratio of 5, but locally ranged up to 27 near the inlet.

3 The submarine experiments displayed no consistent relationship between either braiding index or bar aspect ratio and the inlet condition or the ratio of flow to sediment discharge.

4 The timescales for channel aggradation, lateral migration and avulsion inform a new stratigraphic model for submarine braided channels, and suggest relatively low vertical persistence of channel bodies.

ACKNOWLEDGMENTS

Jeff Peakall and Associate Editor Jaco Baas provided constructive reviews. The SAFL Industrial Consortium supported this work. Jeff Marr, Rob Gabrielson, and Ben Erickson helped to design the basin, and David Baldus helped conduct the experiments. Charles Nguyen and Patrick Arnold provided computing support. Experiment methods are archived through the Sediment Experimentalist Network (http://www.sedexp.net/). Topography, image and flow model data are available at the Digital Repository for the University of Minnesota (https://doi.org/10.13020/D6R088).

REFERENCES

Abreu, V., **Sullivan, M.**, **Pirmez, C.** and **Mohrig, D.** (2003) Lateral accretion packages (LAPs): an important reservoir element in deep water sinuous channels. *Mar. Petrol. Geol.*, **20**, 631–648.

Allen, J.R.L. (1979) Studies in fluviatile sedimentation: an elementary geometrical model for the connectedness of avulsion-related channel sand bodies. *Sed. Geol.*, **24**, 253–267.

Ashmore, P.E. (1982) Laboratory modelling of gravel braided stream morphology. *Earth Surf. Proc. Land.*, **7**, 201–225.

Ashmore, P. (2013) 9.17 Morphology and dynamics of braided rivers. In: *Treatise on Geomorphology* (Eds J.

Shroder and E. Wohl), **9**, pp. 289–312, Academic Press, San Diego, CA.

Ashworth, P., **Best, J.L.**, **Leddy, J.O.** and **Geehan, G.W.** (1994) The physical modelling of braided rivers and deposition of fine-grained sediment. In: *Process Models and Theoretical Geomorphology* (Ed. M.J. Kirby), pp. 115–139. John Wiley and Sons, Chichester.

Ashworth, P.J., **Best, J.L.** and **Jones, M.A.** (2007) The relationship between channel avulsion, flow occupancy and aggradation in braided rivers: insights from an experimental model. *Sedimentology*, **54**, 497–513.

Asvadi, A., **Mahdavinataj, H.**, **Karami, M.** and **Baleghi, Y.** (2014) Incremental discriminative color object tracking. In: *Artificial Intelligence and Signal Processing* (Eds A. Movaghar, M. Jamzad and H. Asadi), *Commun. Comput. Inform. Sci.*, **427**, 71–81.

Bates, P.D., **Horritt, M.S.** and **Fewtrell, T.J.** (2010) A simple inertial formulation of the shallow water equations for efficient two-dimensional flood inundation modelling. *J. Hydrol.*, **387**, 33–45.

Belderson, R.H., **Kenyon, N.H.**, **Stride, A.H.** and **Pelton, C.D.** (1984) A "braided" distributary system on the Orinoco deep-sea fan. *Mar. Geol.*, **56**, 195–206.

Bertoldi, W., **Zanoni, L.** and **Tubino, M.** (2009) Planform dynamics of braided streams. *Earth Surf. Proc. Land.*, **34**, 547–557.

Braun, J. and **Sambridge, M.** (1997) Modelling landscape evolution on geological time scales: a new method based on irregular spatial discretization. *Basin Res.*, **9**, 27–52.

Bridge, J.S. and **Lunt, I.A.** (2006) Depositional models of braided rivers. In: *Braided Rivers: Processes, Deposits, Ecology and Management* (Eds G.H. Sambrook Smith, J.L. Best, C.S. Bristow and G.E. Petts), *IAS Spec. Publ.*, **36**, 11–50.

Bridge, J.S. and **Mackey, S.D.** (1993) A theoretical study of fluvial sandstone body dimensions. *Spec. Publ. Int. Assoc. Sedimentol.*, **15**, 213–216.

Callec, Y., **Deville, E.**, **Desaubliaux, G.**, **Griboulard, R.**, **Huyghe, P.**, **Mascle, A.**, **Mascle, G.**, **Noble, M.**, **Padron de Carillo, C.** and **Schmitz, J.** (2010) The Orinoco turbidite system: tectonic controls on sea-floor morphology and sedimentation. *AAPG Bull.*, **94**, 869–887.

Cazanacli, D., **Paola, C.** and **Parker, G.** (2002) Experimental steep, braided flow: application to flooding risk on fans. *J. Hydraul. Eng.*, **128**, 322–330.

Chow, V.T. (1959) *Open Channel Hydraulics*. McGraw-Hill, New York, NY.

Clark, J.D., **Kenyon, N.H.** and **Pickering, K.T.** (1992) Quantitative analysis of the geometry of submarine channels: implications for the classification of submarine fans. *Geology*, **20**, 633–636.

Coulthard, T. (2017) CAESAR-Lisflood 1.9b [Data set]. Zenodo. Available at: https://doi.org/10.5281/zenodo.321820.

Coulthard, T.J., **Neal, J.C.**, **Bates, P.D.**, **Ramirez, J.**, **de Almeida, G.A.M.** and **Hancock, G.R.** (2013) Integrating the LISFLOOD-FP 2D hydrodynamic model with the CAESAR model: implications for modelling landscape evolution. *Earth Surf. Proc. Land.*, **38**, 1897–1906.

Covault, J.A. and **Graham, S.A.** (2010) Submarine fans at all sea-level stands: tectono-morphologic and climatic controls on terrigenous sediment delivery to the deep sea. *Geology*, **38**, 939–942.

Cronin, B.T. and **Kidd, R.B.** (1998) Heterogeneity and lithotype distribution in ancient deep-sea canyons: point Lobos deep-sea canyon as a reservoir analogue. *Sed. Geol.*, **115**, 315–349.

Deptuck, M.E., **Sylvester, Z.**, **Pirmez, C.** and **O'Byrne, C.** (2007) Migration–aggradation history and 3-D seismic geomorphology of submarine channels in the Pleistocene Benin-major Canyon, western Niger Delta slope. *Mar. Petrol. Geol.*, **24**, 406–433.

Egozi, R. and **Ashmore, P.** (2008) Defining and measuring braiding intensity. *Earth Surf. Proc. Land.*, **33**, 2121–2138.

Egozi, R. and **Ashmore, P.** (2009) Experimental analysis of braided channel pattern response to increased discharge. *J. Geophys. Res.*, **114**(F2), F02012.

Flood, R.D. and **Damuth, J.E.** (1987) Quantitative characteristics of sinuous distributary channels on the Amazon Deep-Sea Fan. *Geol. Soc. Am. Bull.*, **98**, 728–738.

Foreman, B.Z., **Lai, S.Y.J.**, **Komatsu, Y.** and **Paola, C.** (2015) Braiding of submarine channels controlled by aspect ratio similar to rivers. *Nature Geosci.*, **8**, 700–703.

Gamberi, F. and **Marani, M.** (2011) Geomorphology and sedimentary processes of a modern confined braided submarine channel belt (Stromboli slope valley, southeastern Tyrrhenian Sea). *J. Sed. Res.*, **81**, 686–701.

García, M.H. and **Parsons, J.D.** (1996) Mixing at the front of gravity currents. *Dynam. Atmos. Oceans*, **24**, 197–205.

Hajek, E.A., **Heller, P.L.** and **Sheets, B.A.** (2010) Significance of channel-belt clustering in alluvial basins. *Geology*, **38**, 535–538.

Heezen, B.C. and **Ewing, M.** (1952) Turbidity currents and submarine slumps, and the 1929 Grand Banks earthquake. *Am. J. Sci.*, **250**, 849–878.

Hein, F.J. and **Walker, R.G.** (1982) The Cambro-Ordovician Cap Enragé Formation, Québec, Canada: conglomeratic deposits of a braided submarine channel with terraces. *Sedimentology*, **29**, 309–352.

Hesse, R., **Klaucke, I.**, **Khodabakhsh, S.**, **Piper, D.J.W.**, **Ryan, W.B.F.** and NAMOC Study Group (2001) Sandy submarine braid plains: potential deep-water reservoirs. *AAPG Bull.*, **85**, 1499–1521.

Huang, H., **Imran, J.** and **Pirmez, C.** (2005) Numerical model of turbidity currents with a deforming bottom boundary. *J. Hydraul. Eng.*, **131**, 283–293.

Jerolmack, D.J. and **Mohrig, D.** (2007) Conditions for branching in depositional rivers. *Geology*, **35**, 463–466.

Jerolmack, D.J. and **Paola, C.** (2007) Complexity in a cellular model of river avulsion. *Geomorphology*, **91**, 259–270.

Jobe, Z.R., **Howes, N.C.** and **Auchter, N.C.** (2016) Comparing submarine and fluvial channel kinematics: implications for stratigraphic architecture. *Geology*, **44**, 931–934.

Kenyon, N.H. and **Millington, J.** (1995) Contrasting deep-sea depositional systems in the Bering Sea. In: *Atlas of Deep Water Environments* (Eds K.T. Pickering, R.N. Hiscott, N.H. Kenyon, F.R. Lucchi and R.D.A. Smith), pp. 196–202. Chapman and Hall, London.

Kneller, B. and **Buckee, C.** (2000) The structure and fluid mechanics of turbidity currents: a review of some recent studies and their geological implications. *Sedimentology*, **47**(Suppl. 1), 62–94.

Konsoer, K., **Zinger, J.** and **Parker, G.** (2013) Bankfull hydraulic geometry of submarine channels created by turbidity currents: relations between bankfull channel characteristics and formative flow discharge. *J. Geophys. Res. Earth Surf.*, **118**, 216–228.

Kuenen, P.H. (1951) Properties of turbidity currents of high density. *SEPM Spec. Publ.*, **2**, 14–33.

Lague, D., **Crave, A.** and **Davy, P.** (2003) Laboratory experiments simulating the geomorphic response to tectonic uplift. *J. Geophys. Res.*, **108**, ETG 3-1–ETG 3-20.

Lai, S.Y.J., **Hung, S.S.C.**, **Foreman, B.Z.**, **Limaye, A.B.**, **Grimaud, J.L.** and **Paola, C.** (2017) Stream power controls the braiding intensity of submarine channels similarly to rivers. *Geophys. Res. Lett.*, **44**, 5062–5070.

Lajeunesse, E., **Malverti, L.**, **Lancien, P.**, **Armstrong, L.**, **Metivier, F.**, **Coleman, S.**, **Smith, C.E.**, **Davies, T.**, **Cantelli, A.** and **Parker, G.** (2010) Fluvial and submarine morphodynamics of laminar and near-laminar flows: a synthesis. *Sedimentology*, **57**, 1–26.

Laval, A., **Cremer, M.**, **Beghin, P.** and **Ravenne, C.** (1988) Density surges: two-dimensional experiments. *Sedimentology*, **35**, 73–84.

Leeder, M.R. (1977) A quantitative stratigraphic model for alluvium, with special reference to channel deposit density and interconnectedness. *Can. Soc. Petrol. Geol. Mem.*, **5**, 587–596.

Limaye, A.B. (2017) Extraction of multithread channel networks with a reduced-complexity flow model. *J. Geophys. Res. Earth Surf.*, **122**, 1972–1990.

Malverti, L., **Lajeunesse, E.** and **Métivier, F.** (2008) Small is beautiful: upscaling from microscale laminar to natural turbulent rivers. *J. Geophys. Res.*, **113**(F4), F04004.

Marr, J.G., **Harff, P.A.**, **Shanmugam, G.** and **Parker, G.** (2001) Experiments on subaqueous sandy gravity flows: the role of clay and water content in flow dynamics and depositional structures. *Geol. Soc. Am. Bull.*, **113**, 1377–1386.

Métivier, F., **Gaudemer, Y.**, **Tapponnier, P.** and **Klein, M.** (1999) Mass accumulation rates in Asia during the Cenozoic. *Geophys. J. Int.*, **37**, 280–318.

Métivier, F., **Lajeunesse, E.** and **Cacas, M.-C.** (2005) Submarine canyons in the bathtub. *J. Sed. Res.*, **75**, 6–11.

Middleton, G.V. (1967) Experiments on density and turbidity currents: III. Deposition of sediment. *Can. J. Earth Sci.*, **4**, 475–505.

Molnar, P. (2004) Late Cenozoic increase in accumulation rates of terrestrial sediment: how might climate change have affected erosion rates? *Annu. Rev. Earth Planet. Sci.*, **32**, 67–89.

Moreton, D.J., **Ashworth, P.J.** and **Best, J.L.** (2002) The physical scale modelling of braided alluvial architecture and estimation of subsurface permeability. *Basin Res.*, **14**, 265–285.

Mosley, M.P. (1982) Analysis of the effect of changing discharge on channel morphology and instream uses in a braided river, Ohau River, New Zealand. *Water Resour. Res.*, **18**, 800–812.

Mulder, T. and **Syvitski, J.P.M.** (1995) Turbidity currents generated at river mouths during exceptional discharges to the world oceans. *J. Geol.*, **103**, 285–299.

Mulder, T., **Savoye, B.** and **Syvitski, J.P.M.** (1997) Numerical modelling of a mid-sized gravity flow: the 1979 Nice turbidity current (dynamics, processes, sediment budget and seafloor impact). *Sedimentology*, **44**, 305–326.

Nakajima, T., **Peakall, J.**, **McCaffrey, W.D.**, **Paton, D.A.** and **Thompson, P.J.P.** (2009) Outer-bank bars: a new intra-channel architectural element within sinuous submarine slope channels. *J. Sed. Res.*, **79**, 872–886.

Nikuradse, J. (1933) Laws of flow in rough pipes. *National Advisory Committe for Aeronautics, Technical Memorandum 1292*.

Normark, W.R. (1970) Growth patterns of deep-sea fans. *AAPG Bull.*, **54**, 2170–2195.

Normark, W.R. and **Piper, D.J.W.** (1991) Initiation processes and flow evolution of turbidity currents: implications for the depositional record. In: *From Shoreline to Abyss* (Ed. R.H. Osborne), *SEPM Special Publication*, **46**, 207–230.

Normark, W.R. and **Reid, J.A.** (2003) Extensive deposits on the Pacific plate from late Pleistocene North American glacial lake outbursts. *J. Geol.*, **111**, 617–637.

Paola, C. (2000) Quantitative models of sedimentary basin filling. *Sedimentology*, **47**(Suppl. 1), 121–178.

Paola, C., **Heller, P.L.** and **Angevine, C.L.** (1992) The large-scale dynamics of grain-size variation in alluvial basins, 1: theory. *Basin Res.*, **4**, 73–90.

Parker, G. (1976) On the cause and characteristic scales of meandering and braiding in rivers. *J. Fluid Mech.*, **76**, 457–480.

Parker, G., **Garcia, M.**, **Fukushima, Y.** and **Yu, W.** (1987) Experiments on turbidity currents over an erodible bed. *J. Hydraul. Res.*, **25**, 123–147.

Passalacqua, P., **Do Trung, T.**, **Foufoula-Georgiou, E.**, **Sapiro, G.** and **Dietrich, W.E.** (2010) A geometric framework for channel network extraction from lidar: nonlinear diffusion and geodesic paths. *J. Geophys. Res.*, **115**(F1), F01002.

Peakall, J., **Ashworth, P.**, **Best, J.**, **Rhoads, B.L.** and **Thorn, C.E.** (1996) Physical modelling in fluvial geomorphology: principles, applications and unresolved issues. In: *The Scientific Nature of Geomorphology* (Eds B.L. Rhoads and C.E. Thorn), pp. 221–253. John Wiley and Sons Ltd, Chichester.

Peakall, J., **McCaffrey, B.** and **Kneller, B.** (2000) A process model for the evolution, morphology, and architecture of sinuous submarine channels. *J. Sed. Res.*, **70**, 434–448.

Peakall, J., **Amos, K.J.**, **Keevil, G.M.**, **William Bradbury, P.** and **Gupta, S.** (2007) Flow processes and sedimentation in submarine channel bends. *Mar. Petrol. Geol.*, **24**, 470–486.

Piper, D.J.W. and **Normark, W.R.** (2009) Processes that initiate turbidity currents and their influence on turbidites: a marine geology perspective. *J. Sed. Res.*, **79**, 347–362.

Pirmez, C. and **Imran, J.** (2003) Reconstruction of turbidity currents in Amazon Channel. *Mar. Petrol. Geol.*, **20**, 823–849.

Prélat, A., **Covault, J.A.**, **Hodgson, D.M.**, **Fildani, A.** and **Flint, S.S.** (2010) Intrinsic controls on the range of volumes, morphologies, and dimensions of submarine lobes. *Sed. Geol.*, **232**, 66–76.

Redolfi, M., **Tubino, M.**, **Bertoldi, W.** and **Brasington, J.** (2016) Analysis of reach-scale elevation distribution in braided rivers: definition of a new morphologic indicator and estimation of mean quantities. *Water Resour. Res.*, **52**, 5951–5970.

Robertson-Rintoul, M.S.E. and **Richards, K.S.** (1993) Braided-channel pattern and palaeohydrology using an index of total sinuosity. *Geol. Soc. London Spec. Publ.*, **75**, 113–118.

Romans, B.W., **Normark, W.R.**, **McGann, M.M.**, **Covault, J.A.** and **Graham, S.A.** (2009) Coarse-grained sediment delivery and distribution in the Holocene Santa Monica Basin, California: implications for evaluating source-to-sink flux at millennial time scales. *Geol. Soc. Am. Bull.*, **121**, 1394–1408.

Rotzien, J.R., **Lowe, D.R.** and **Schwalbach, J.R.** (2014) Processes of sedimentation and stratigraphic architecture of deep-water braided lobe complexes: the Pliocene repetto and Pico formations, ventura basin, USA. *J. Sed. Res.*, **84**, 910–934.

Rowland, J.C., **Hilley, G.E.** and **Fildani, A.** (2010) A test of initiation of submarine leveed channels by deposition alone. *J. Sed. Res.*, **80**, 710–727.

Sapozhnikov, V. and **Foufoula-Georgiou, E.** (1996) Self-affinity in braided rivers. *Water Resour. Res.*, **32**, 1429–1439.

Sømme, T.O., **Helland-Hansen, W.**, **Martinsen, O.J.** and **Thurmond, J.B.** (2009) Relationships between morphological and sedimentological parameters in source-to-sink systems: a basis for predicting semi-quantitative characteristics in subsurface systems. *Basin Res.*, **21**, 361–387.

Straub, K.M. and **Mohrig, D.** (2008) Quantifying the morphology and growth of levees in aggrading submarine channels. *J. Geophys. Res.*, **113**(F3), F03012.

Straub, K.M., **Mohrig, D.**, **McElroy, B.**, **Buttles, J.** and **Pirmez, C.** (2008) Interactions between turbidity currents and topography in aggrading sinuous submarine channels: a laboratory study. *Geol. Soc. Am. Bull.*, **120**, 368–385.

Tal, M. and **Paola, C.** (2010) Effects of vegetation on channel morphodynamics: results and insights from laboratory experiments. *Earth Surf. Proc. Land.*, **35**, 1014–1028.

Tarboton, D.G. (1997) A new method for the determination of flow directions and upslope areas in grid digital elevation models. *Water Resour. Res.*, **33**, 309–319.

Walker, R.G. (1978) Deep-water sandstone facies and ancient submarine fans: models for exploration for stratigraphic traps. *AAPG Bull.*, **62**, 932–966.

Weimer, P. and **Link, M.H.** (1991) Global petroleum occurrences in submarine fans and turbidite systems. In: *Frontiers in Sedimentary Geology, Seismic Facies and Sedimentary Processes of Submarine Fans and Turbidite Systems* (Eds P. Weimer and M.H. Link), pp. 9–67. Springer-Verlag, New York, NY.

Welber, M., **Bertoldi, W.** and **Tubino, M.** (2012) The response of braided planform configuration to flow variations, bed reworking and vegetation: the case of the Tagliamento River, Italy. *Earth Surf. Proc. Land.*, **37**, 572–582.

Willis, B. (1993) Ancient river systems in the Himalayan foredeep, Chinji Village area, northern Pakistan. *Sed. Geol.*, **88**, 1–76.

Wynn, R.B., **Cronin, B.T.** and **Peakall, J.** (2007) Sinuous deep-water channels: genesis, geometry and architecture. *Mar. Petrol. Geol.*, **24**, 341–387.

Xu, J.P. (2010) Normalized velocity profiles of field-measured turbidity currents. *Geology*, **38**, 563–566.

Yu, B., **Cantelli, A.**, **Marr, J.**, **Pirmez, C.**, **O'Byrne, C.** and **Parker, G.** (2006) Experiments on self-channelized subaqueous fans emplaced by turbidity currents and dilute mudflows. *J. Sed. Res.*, **76**, 889–902.

Manuscript received 21 June 2017; revision accepted 11 January 2018

Supporting Information

Additional Supporting Information may be found in the online version of this article:

Movie S1 (ms01.mp4). Movie of experiment Submarine 1.

Movie S2 (ms02.mp4). Movie of experiment Submarine 3.